Institute of Space Systems
University of Stuttgart

Kinetic modelling of the jet extraction mechanism in spherical IEC devices

IRS-13-P06

Final Report

Authors:
Georg Herdrich[1], Dejan Petkow[2], Constanze Syring[1], Marcel Pfeiffer[1]

Affiliations:
[1]Universität Stuttgart, Institute of Space Systems (IRS), Pfaffenwaldring 29, 70569 Stuttgart, Germany
[2]ESA ACT

Date: 14.10.2013

Contacts:

PD Dr.-Ing. Georg Herdrich
Tel: +49 (0)711 / 6856 2412
Fax: +49 (0)711 / 6856 3596
e-mail: herdrich@irs.uni-stuttgart.de

Leopold Summerer (Technical Officer)
Tel: +31(0)715654192
Fax: +31(0)715658018
e-mail: act@esa.int

Available on the ACT website
http://www.esa.int/act

Ariadna ID: 12/3201
Ariadna study type: Standard
Contract Number: 4000106092/12/NL/KML

Scope

This document contains the final report of the Ariadna study 12/3201 ”Kinetic modeling of the jet extraction mechanism in spherical IEC devices”. The study aims at resolving numerically the effects and phenomena leading to and occurring in a jet extraction inside a spherical Inertial Electrostatic Confinement device. The underlying numerical methodology and software is based on a Particle-In-Cell (PIC) code solving the full set of Maxwell equations coupled with a) a Direct simulation Monte Carlo (DSMC) solver which resolves (mainly, but not only) chemical processes like electron induced ionisaton of atoms, and with b) a Monte Carlo based Fokker Planck solver (embedded in the DSMC solver) which resolves the Coulomb collision induced relaxation of electron and ion velocity distribution functions.
Due to the extremely low time step size necessary to guarantee numerical stability of the PIC solver the simulation domain is downsized. This speed-up process demands the definition of proper inflow boundary conditions. These conditions are derived on basis of available literature and scaling laws. Other main speed-up measures are neglecting of Coulomb collisions as well as ionisation processes. Different spatial and particle resolutions are tested before completing a full simulation. Estimations for further simulations and studies are given and more detailed simulations of the jet are proposed.

Contents

List of Figures

List of Tables

List of Abbreviations

BC	Boundary Conditions
CMC	Continuum Monte Carlo
DG-SEM	Discontinuous Galerkin Spectral Element Method
DOF	Degrees of Freedom
DSMC	Direct Simulation Monte Carlo
FP	Fokker Planck
HLRS	High Performance Computing Center Stuttgart
IAG	Institute of Aerodynamics and Gas Dynamics
IEC	Inertial Electrostatic Confinement
IRS	Institute of Space Systems
KIT	Karlsruhe Institute of Technology
OF	OpenFoam
PIC	Particle in Cell
SF	Shape Functions
VTK	Visualization Toolkit

1 Introduction

The inertial electrostatic confinement (IEC) of ions for the purpose of creating a high density (fusion) plasma, originally proposed by Farnsworth [1], was first studied experimentally by Hirsch [2] in 1967. However little was done to study this concept until R.W. Bussard [3] and G.H. Miley [4] renewed studies in the early 1990s. There are several design types of IECs, e.g. single-grid devices [5], multiple-grid designs [6] or a hybrid magnetic-electrostatic version [3]. All these experiments are fusion power concepts, yet no break-even for the energy production is expected from the concepts introduced here. But due to the design simplicity and scalability, development was still pursued and research done over decades aimed to increase the fusion rates as much as possible, so that they can be used e.g. as commercial neutron sources [7] as it was planned by Daimler-Chrysler Aerospace (IEC star-mode fusion neutron source, R&D). Today, Gradel sarl (Project "NSD Gradel Fusion", formerly the NSD Fusion GmbH) pushes in Europe the enhancement of commercial IEC devices amongst other things for luggage inspections or neutron radiography.
With the beginning of 2010, a project was set up to build up an IEC test stand in the IRS Laboratory which shall help to broaden the understanding and knowledge about inertial electrostatic plasma confinement and related plasma beam extraction [8]. Moreover, a plasma simulation tool for investigating highly rarefied gas and plasma flows is permanently under development since 2004/05 and applied to study phenomena leading to the plasma jet extraction.
Available scientific literature on IEC with and without jet extraction states that grid transparency is increased with respect to what is state of the art in gridded ion thrusters, thus promising lower grid erosion and, hence, increased life times. However, literature on IEC in jet mode contains very little details regarding the underlying physics which lead to the jet extraction. Even worse, a comprehensive experimental jet characterisation allowing to derive reliable comparative conclusions (with respect to state of the art electric propulsion devices) is currently not available. Correspondingly, not only jet extraction is not really understood, but also stated thruster properties contain a significant portion of speculation and anticipation. It is the intention of this study to improve our understanding of the IEC technology and certainly of the jet extraction mechanism as key to the IEC's usability as a space propulsion device. The method of choice is to apply a numerical code which is able to resolve the relevant physics with adequate accuracy.

Inertial Electrostatic Confinement and Operational Modes

The following section gives an overview of inertial electrostatic confinement theory as well as the assumed underlying particle extraction mechanism.

Plasma Confinement Working Principle

The first IEC reactor was invented by Farnsworth [9]. He called this concept Fusor and it consisted of two concentric grids. Ions generated by ion guns got accelerated between these grids into the center where they collided and some of them fused due to the high energies of the fuel ions.
This type of reactor was later enhanced towards the Hirsch-Farnsworth reactor [2], see Fig. 1.1. A spherical, concentric and strongly negatively biased grid is placed in a grounded, evacuated, spherical chamber. The grid is the cathode, the chamber wall the anode. The chamber will be flooded with a fuel. By a glow discharge between anode and cathode, ions can be generated which will then be accelerated to the grid center. Occasionally, fusion processes can be measured. But the majority of ions doesn't take part in a fusion process and leaves the grid center. Due to the potential gradient between cathode and anode they become slower again and get accelerated back into the center.

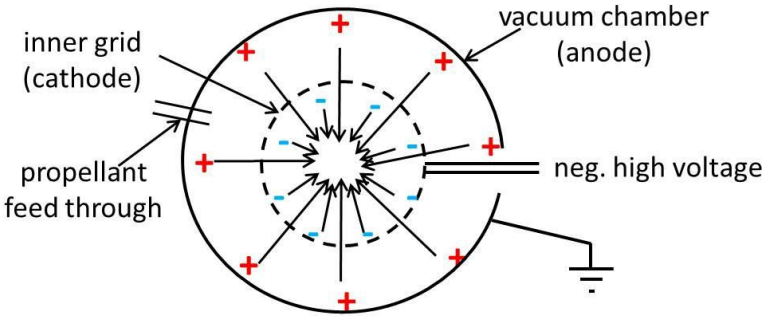

Figure 1.1: General setup of Hirsch-Farnsworth reactor [2].

Operational Modes

The star mode was discovered by G.Miley [4] at the University of Illinois, see Fig. 1.2 (a). This mode of operation can be achieved under certain conditions with a symmetrical cathode grid. It has a fairly symmetrical flow of particles going through the cathode grid. For a given grid design and dimensions, an operational window exists where high density beams will form, initiating the star mode of operation. Care in grid

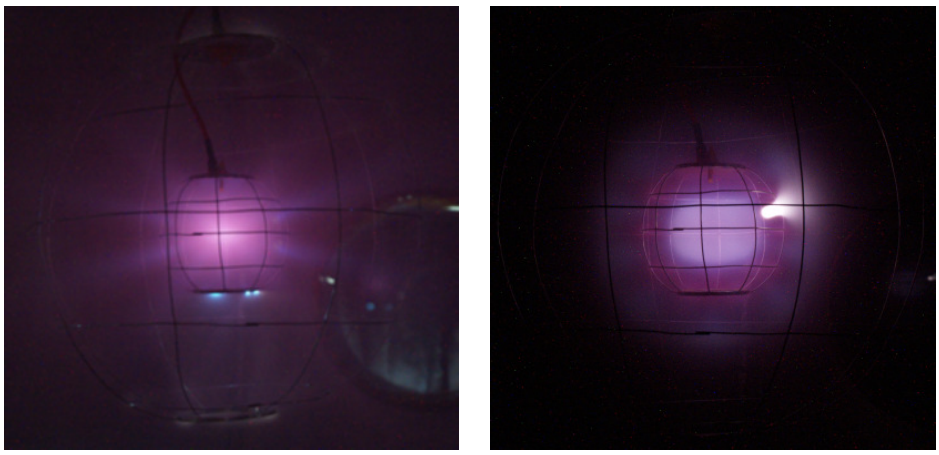

(a) Star Mode (b) Jet Mode

Figure 1.2: Operation modes at IRS IEC device.

design and manufacturing, especially large grid openings, is required for this mode, but all openings in the grid have the same size. This phenomenon is explained in detail in [10].
Figure 1.3 displays the equal potential lines of a cross-sectional cut through the center of a spherical particle-free grid system[1] showing the potential distribution between these grids. For the sake of simplicity, the mesh wires and openings were not modeled as such. Instead, their geometrical alignment was replaced by spheres having one opening each, representing the (enlarged) opening for jet extraction. The potential distribution in the cathode's opening indicates the existence of electric fields which enable some electrons to overcome the potential barrier (and thereby dragging ions). Due to the convex equipotential surfaces there is an area inside the cathode which is at higher potential than the cathode. In fact, the cathode wires lead to those potential surfaces in each mesh opening. When the electrons exit the inner cathode space they encounter the concave potential field lines which force them on a constricted beam path. This results in a star like pattern coming from the grid openings. The electrons cause significant ionisation of the background gas creating ions [10] in the produced beams. Thereby generated ions in turn get accelerated by the cathode potential into the cathode center. They tend to stay on their beam path while oscillating through the cathode due to their birth orientation and negative space charge potential caused by the beam electrons.
Nevertheless through these beams high energy ions originated in the ionisation zone near the cathode will not leave the system. In order to allow high energy ions to escape the system through a beam (jet mode, see Fig. 1.2 (b)), researchers at the University of Illinois [10] increased the perturbation of the potential field at the grid by enlarging one grid opening more than the others. The enlarged hole destroys some of the symmetry of the spherical grid field. This allows for electrons originating from e.g.

[1] Simulations performed with OpenFOAM.

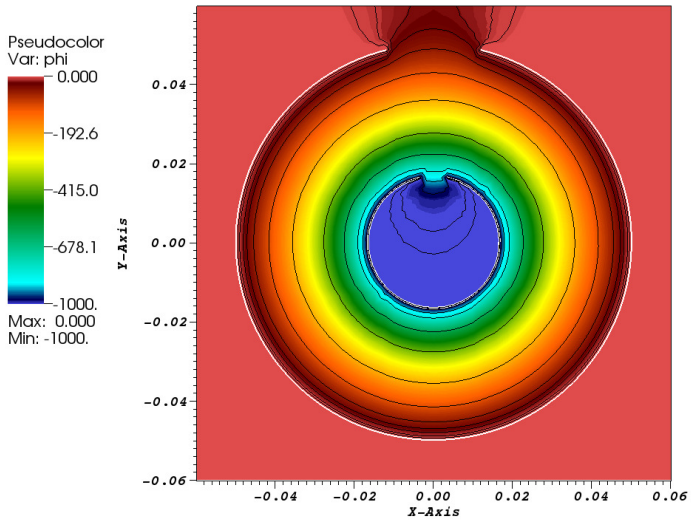

Figure 1.3: OpenFoam Simulation (cut through center of spherical grid system): Potential field distribution between grids without particles ($V_g = -1kV$).

ionisation with the background gas to flow out of the cathode as in the micro channels mentioned above. It is speculated that they, in turn, drag high energy ions from the cathode center to follow the electrons. In [11] it was investigated that the extracted beam contains high energy ions but still significantly less than low energy ions which have been generated by electrons ionising background gas between anode and cathode. By adding a guide grid to the grid outlet as proposed in [12], which has a slightly higher potential than the cathode grid, the extraction of more high energy ions could be facilitated.

IEC Device at IRS

The IEC device which is being build up at IRS is not a direct reference for this study. However, there are similarities between this design and the simulation's configuration which is advantageous when planning test campaigns for measuring electron densities and comparing with simulation data. This will also facilitate the usage of obtained plasma parameters for later simulations where simulation parameters for inflow and boundary condition definition are more reliably then in this study.
The device configuration chosen at IRS is a spherical, concentric two-grid system since the used vacuum tank is not spherical. The first grid setup that was manufactured, has an anode diameter of $30cm$ and a cathode diameter of $10cm$. The anode could not be build larger due to limited manufacturing capabilities. The cathode's diameter is limited in down sizing due to the spatial resolution of diagnostic methods. The grid wire arrangement has the shape of longitude/latitude lines, see Fig. 1.4. Argon is used as propellant due to its availability and facile ionisation and the good

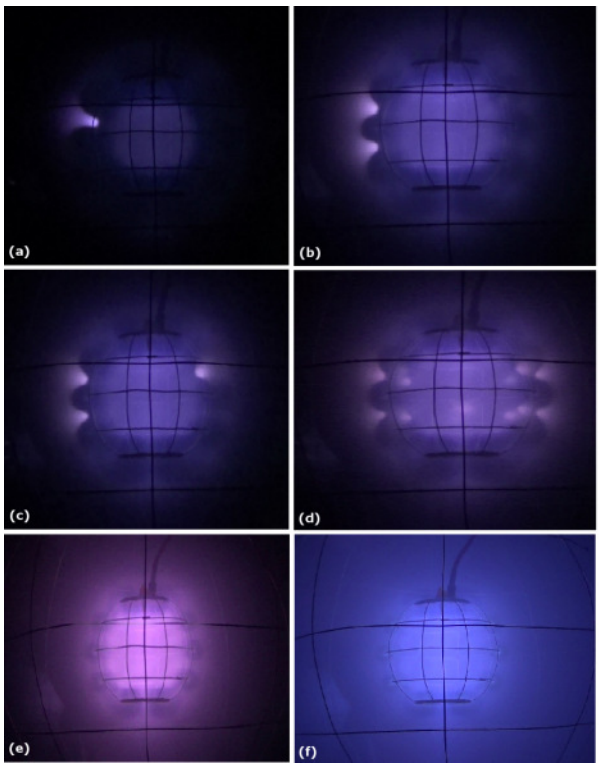

Figure 1.4: Discharge phenomena for the operational discharge conditions with $p_{ch} = 8 \times 10^{-2} mbar$ at IRS IEC

implementation within the simulation tool. Discharge phenomena investigated at IRS [13] show that the operational range where one jet is extracted seems to be controlled by applied voltages and flowing current and is therefore limited to certain operational conditions, see Tab. 1.1. This makes the assessment of physical mechanisms - leading to a jet extraction for space propulsion applications - even more important.

Table 1.1: Operational discharge conditions at $p_{ch} = 8 \times 10^{-2} mbar$ at IRS IEC.

Fig. 1.4	Voltage $[kV]$	Current $[mA]$
a	0.26	0.9
b	0.4	9.8
c	0.44	13.3
d	0.49	18.4
e	0.63	40
f	0.76	60

Report structure

Chapter 2 gives an introduction to the used simulation tool and the coupling between the different solvers. Input parameters as particle densities, temperatures and velocities are derived in chapter 3 while a reference setup for the grid generation and the assessment of potential boundary conditions with OpenFOAM are presented in chapter 4. Preparatory studies investigating the necessary spatial and particle resolution, the necessity of shape functions and the consideration of ionisation processes are discussed in chapter 5. Chapter 6 provides simulation results and respective interpretation of the data. Chapter 7 provides a summary of the central activities as well as conclusions on the results obtained. The report closes with an outlook, see chapter 8.

2 Simulation Software Framework

In 2005, an academic cooperation were founded between the Institute of Aerodynamics and Gas Dynamics (IAG) of the Universitaet Stuttgart, the High Performance Computing Center Stuttgart (HLRS), the Institute of Space Systems (IRS) of the Universitaet Stuttgart, and the Karlsruhe Institute of Technology (KIT). The goal was to numerically study the acceleration phenomena inside a non-stationary magneto-plasma-dynamic thruster [14]. Due to certain thruster properties the main software requirements were identified as follows:

1. 3D capability is needed,
2. fully kinetic solution approach,
3. particles are treated relativistically,
4. the full set of Maxwell equations is solved,
5. chemistry is considered, and
6. collisional relaxation of electrons and ions is modeled.

The term *fully kinetic* implies that, as in most kinetic approaches, the plasma is represented by a sample of different species of charged particles. In each time step the electromagnetic fields obtained by the numerical solution of the Maxwell equations at the grid are interpolated to the actual locations of these particles. According to the Lorentz force the charges are redistributed and the new phase-space coordinates are determined by solving the usual laws of dynamics. To close the chain of self-consistent interplay, the particles have to be located with respect to the computational grid in order to assign the contribution of each charged particle to the charge and current density at the nodes which are the sources for the Maxwell equations in the subsequent time step. Given that, the presented approach is a combination of two different frameworks:

- Eulerian framework: discretisation of Maxwell's equations,
- Lagrangian framework: discretisation of the species' distribution functions.

These frameworks are coupled and interact with each other via the charge-to-grid and force-to-charge assignment steps.
Such a basic scheme is the starting point to build up the necessary program structure of the coupled code which allows for flexible combination of different modules and extensions. In fact, our code is able to solve kinetically the complete and fundamental gas kinetic equation which will be briefly introduced in the next section.

2.1 Governing equations and code coupling

The governing equation for rarefied gases and plasmas is the Boltzmann equation

$$\frac{\partial f_\alpha}{\partial t} + \mathbf{v}\frac{\partial f_\alpha}{\partial \mathbf{x}} + \frac{\mathbf{F}}{m_\alpha}\frac{\partial f_\alpha}{\partial \mathbf{v}} = \int_{-\infty}^{\infty}\int_{0}^{4\pi} \left[f_\alpha(\mathbf{v}')f_\beta(\mathbf{w}') - f_\alpha(\mathbf{v})f_\beta(\mathbf{w})\right] g\sigma_D \mathrm{d}\Omega\mathrm{d}\mathbf{v}. \tag{2.1}$$

which describes the evolution of the velocity distribution function f_α of species α scattered by a background species β. The left side of Eq. (2.1) describes the change of f_α over time t, the dependence of f_α on spatial inhomogenities, and the change of f_α as a consequence of external (i.e. non-collisional) forces $\mathbf{F}$ accelerating the particles with the mass m_α. The right side of Eq. (2.1) describes the change of f_α due to inter-particle collisions. Collisions are described by the collision cross section σ_D which depends on the relative velocity $g = |\mathbf{v} - \mathbf{w}|$ between both particles. Post-collisional quantities are primed.
The mathematical treatment of the Boltzmann equation is extremely difficult [15, 16, 17]. The common approach is to split Eq. (2.1) in corresponding domains simply because the dominating physical processes are defined by certain temporal and spatial scales. Ignoring the collisional processes reduces the Boltzmann equation to the Vlasov equation which, in combination with the force information, describes collective plasma phenomena. Those are defined on scales *above* the so-called Debye length. The most established kinetic solver type is the Particle In Cell (PIC) approach (see e.g. [18]) which is also applied in this study.
Collisional processes can be characterised by the mean collision time τ which typically follows the following order:

$$\overbrace{\tau_{ee} < \tau_{ei} < \tau_{ii}}^{small\ angle\ scattering} \quad < \quad \underbrace{\tau_{en} < \tau_{in} < \tau_{nn}}_{large\ angle\ scattering} . \tag{2.2}$$

The indices describe the charge related nature of the particles (i.e. *e*lectron, *i*on, *n*eutral). As can be seen in Eq. (2.2) the order of the collision frequency is related to the scattering angle of a single collision process. Therefore, two different solver types have been established by the corresponding communities: A Fokker Planck (FP) solvers solves the Fokker Planck equation which can be derived from the RHS of Eq. (2.1) assuming small scattering angles. All other scattering processes can be covered kinetically by e.g. the Direct Simualation Monte Carlo (DSMC) approach. Both a Monte Carlo based FP solver and a DSMC solver have been developed in order to resolve all plasma phenomena on all scales by coupling to a PIC solver, see Fig. 2.1. The three different solvers (PIC, DSMC, and FP) are aligned in a parallel fashion describing the mutual independency during the computation. However, each solver produces an information on the change of the particle velocities treated in the respective solver such that, all velocity change contributions are considered.

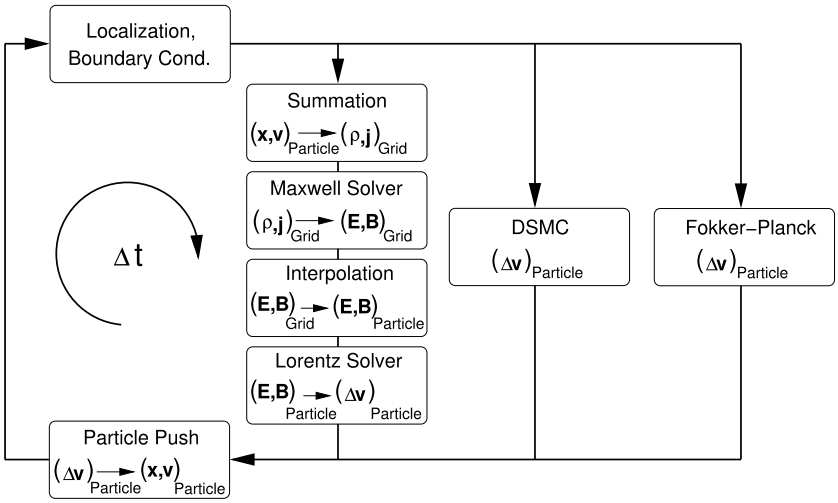

Figure 2.1: Cycle of PICLas time step.

The subsequent sections describe briefly the solvers and some of their major characteristics. For a complete set of information please refer to the references.

2.2 Introduction to the PIC solver

In a plasma, the forces acting on charged particles are described by the Lorentz force

$$\mathbf{F} = q\left[\mathbf{E} + \mathbf{v} \times \mathbf{B}\right] \tag{2.3}$$

with E and B representing electric and magnetic fields on each particle's position. The charge of the particle is defined by q.
The evolution of the electromagnetic field is given by Maxwell's equations:

$$\frac{\partial \mathbf{E}}{\partial t} - c^2 \nabla \times \mathbf{B} = -\frac{\mathbf{j}}{\epsilon_0}, \tag{2.4}$$

$$\frac{\partial \mathbf{B}}{\partial t} + \quad \nabla \times \mathbf{E} = 0, \tag{2.5}$$

$$\nabla \cdot \mathbf{E} = \frac{\rho}{\epsilon_0}, \tag{2.6}$$

$$\nabla \cdot \mathbf{B} = 0. \tag{2.7}$$

which are very well known and not further described here. The source terms

$$\rho(\mathbf{x}, t) = q \int_{\mathbb{R}^3} f(\mathbf{x}, \mathbf{v}, t) \mathrm{d}^3 v,$$

$$\mathbf{j}(\mathbf{x}, t) = q \int_{\mathbb{R}^3} \mathbf{v} f(\mathbf{x}, \mathbf{v}, t) \mathrm{d}^3 v.$$

are the charge and current densities ρ and $\mathbf{j}$. Before applying the advanced solution technique, the four Maxwell equations are transformed to a set of four hyperbolic equations, the pure hyperbolic maxwell (PHM) equations [19]:

$$\begin{aligned}
\frac{\partial \mathbf{E}}{\partial t} - c^2 \nabla \times \mathbf{B} + \chi c^2 \nabla \phi &= -\frac{\mathbf{j}}{\varepsilon_0}, \\
\frac{\partial \mathbf{B}}{\partial t} + \nabla \times \mathbf{E} + \gamma \nabla \psi &= 0, \\
\frac{1}{\gamma c^2} \frac{\partial \psi}{\partial t} + \nabla \cdot \mathbf{B} &= 0, \\
\frac{1}{\chi} \frac{\partial \phi}{\partial t} + \nabla \cdot \mathbf{E} &= \frac{\rho}{\varepsilon_0},
\end{aligned}$$

with the additional divergence cleaning terms ϕ and ψ and the so-called divergence cleaning parameters χ and γ. This means that not only the time dependent Maxwell equations are solved but also the conservation of charge and current is fulfilled even for numerical discrepancies in the divergence calculation. This PHM equation system can be written in the short conservation form [20]:

$$\frac{\partial \mathbf{u}}{\partial t} + \sum_{d=1}^{3} \mathbf{K}_d \frac{\partial \mathbf{u}}{\partial x_d} = \mathbf{g} \tag{2.8}$$

with the state vector $\mathbf{u} = (E_x, E_y, E_z, B_x, B_y, B_z, \psi, \phi)^T$, the source vector $\mathbf{g} = -\frac{1}{\varepsilon_0} (j_x, j_y, j_z, 0, 0, 0, 0, -\chi\rho)^T$ and the corresponding flux matrices $\mathbf{K}_d \in \mathbb{R}^{8\times 8}$. This equation is the starting point of the solution technique described in Sec. 2.2.2. The order of the subsequently following sections is in accordance with the code coupling scheme.

2.2.1 Summation

No matter which numerical scheme is applied to which set of Maxwell equations, in all cases the relevant source terms need to be known on the grid in order to provide input data for the solver. This process is also known as deposition and describes the charge and current (density) deposition from the particle's position to the grid (or corresponding grid points). The lowest order approach for the transfer of charge and current (densities) consists of summing up the contribution of charge and current of all particles within a grid cell and applying the corresponding densities uniformly to all grid nodes within a cell. While this method is fast, it leads to strong oscillations in the source terms due to particles moving between cells. Another popular approach is the Nearest Grid Point scheme in which each source is deposited to the node which is closest to this source. This method is still fast but induces also numerical instabilities.

In order to distribute the charge and current of a particle over a larger volume, thereby reducing the oscillations and allowing a higher order deposition, shape functions are used to approximate a particle cloud. Here, the charges and current densities are deposited partially to the grid nodes based on the shaped distribution function that can be defined over several cells. A good overview of current techniques and implemented solutions can be found in [21] and [22].

2.2.2 Maxwell solver

The 3D transient field solver for Maxwell's equations is based on a discontinuous Galerkin (DG) method including a new approach from the spectral element community called Spectral Element Method (SEM). This approach has shown an even greater potential to save memory and to be very fast. The key features of the DG-SEM scheme can be found in the Lagrangian basis function and the utilisation of a tensor product based algorithm to evaluate the basis function. In the following the theoretical background of the DG-SEM scheme to solve equations of the form (2.8) is briefly introduced. For an in-depth description please refer to [23].
Given the one-dimensional scalar conservation equation without source terms,

$$u_t + f_x(u) = 0, \quad u \in \mathcal{P}_n \tag{2.9}$$

with $u(x,0) = u_0$, $-1 \leq x \leq 1$ and a boundary a variational form is introduced, following the Galerkin approach,

$$\int_{-1}^{1} (u_t + f_x(u))\ \phi\ dx = 0, \tag{2.10}$$

with the test function $\phi = \phi(x) \in \mathcal{P}_n$. The weak form is derived by partial integration yielding

$$\int_{-1}^{1} u_t \phi\ dx + [f(u)\phi]_{-1}^{1} - \int_{-1}^{1} f(u)\phi_x\ dx = 0. \tag{2.11}$$

Furthermore the solution is approximated by the polynomial ansatz:

$$u(x,t) \approx u_h(x,t) = \sum_{j=0}^{\overbrace{N}^{\text{polynomial order}}} \underbrace{\hat{u}_j(t)}_{\text{DOF}}\ \underbrace{\phi_j(x)}_{\text{basis function}} \tag{2.12}$$

and the integrals are approximated by a numerical quadrature rule leading to:

$$\int_{-1}^{1} \phi(x)dx \approx \sum_{k=0}^{N_{GP}-1} \phi(x_k)w_k, \tag{2.13}$$

where x_k are Gauss points, N_{GP} the number of Gauss points and w_k are integration weights. For a conservation equation in 3D, the 3D basis function can be expressed as a tensor product of 1D basis functions, yielding

$$\mathbf{u}(x,y,z,t) \approx \sum_{k=0}^{N}\sum_{l=0}^{N}\sum_{m=0}^{N} \mathbf{u}_{k,l,m}\ \phi_k(x)\ \phi_l(y)\ \phi_m(z). \tag{2.14}$$

Due to the tensor product only 1D operators have to be evaluated in each spatial direction, which allows both an efficient implementation (as in 1D case) and an efficient parallelisation. An optional source term is carried along through the equations above. Further information can also be found in [22].

2.2.3 Interpolation

The interpolation is the inverse step of the summation or deposition step. Thanks to the DG scheme, the solution polynomial (Eq. 2.14) can be evaluated an any position in each cell. This allows to determine $\mathbf{E}(\mathbf{x})$ and $\mathbf{B}(\mathbf{x})$ at each particle's position.

2.2.4 Lorentz solver

In this step, the Lorentz force is calculated according to

$$\mathbf{F} = q\left(\mathbf{E} + \mathbf{v} \times \mathbf{B}\right) \tag{2.15}$$

using field data $\mathbf{E}$ and $\mathbf{B}$ on each particle's position obtained in the previous step. Once $\mathbf{F}$ is known, a simple Euler explicit algorithm is used to calculate the velocity update (or increment) according to

$$\frac{\mathrm{d}\mathbf{v}}{\mathrm{d}t} = \frac{1}{m\gamma}\mathbf{F}. \tag{2.16}$$

Relativistic properties are covered by the relativistic coefficient γ.

2.2.5 Particle Push

The $\triangle\mathbf{v}$ contributions of the individual solvers are summed up and the particles are advanced according to

$$\frac{\mathrm{d}\mathbf{x}}{\mathrm{d}t} = \mathbf{v}. \tag{2.17}$$

Equation (2.17) is solved using a explicit Euler scheme. The algorithm is not only efficient but also accurate due to the fact that the time step size is given by the explicit Maxwell solver which resolves information transport at vacuum speed of light. This guarantees the push algorithm to work stable despite its simplicity.

2.3 Introduction to the DSMC solver

For short range interactions a DSMC solver is applied. This methodology was originally introduced by Bird more than 40 years ago in the context of high enthalpy atmospheric re-entry flow simulation at high altitudes, see e.g. [24]. Under those conditions standard continuum methods fail due to failing assumptions inherent to continuum approaches: that the equilibrium energy distribution function is not more than *slightly* disturbed. A typical measure of the disturbance's strength is commonly expressed by the non-dimensional Knudsen number $Kn = \lambda/L$ where L is some reference length and λ represents the mean free path. Irrespectively of the reference length chosen, high Kn values refer either to rarefied flows (high λ values), or to strong disturbances, or to both. For a broad introduction into the principles of DSMC please refer to [25] and references therein.

2.3.1 Working principle

The basic working principle of DSMC is as follows: Given a proper temporal, spatial, and particle discretisation, each simulation particle is assigned to its corresponding grid cell. Then, particle pairs are formed in each cell. Each particle pair is evaluated according to the collision induced interaction which can be elastic, inelastic, or reactive. In this process, every single interaction type i is evaluated against an equally distributed random number $R \in [0, 1]$ on basis of an individually calculated interaction probability $P_i \in [0, 1]$. Only those interactions are executed where $P_i > R$ with R being always a newly generated random number, and where a potentially existing energy barrier as for dissociation of ionisation can be overcome. Post-collisional state properties are then assigned to the (potentially new) particles which are then moved, localised, and where necessary assigned to their new host cells. Depending on the model's complexity, interactions with solid boundaries can be something between speculiar scattering and chemical reactions including particle adsorption.
Since the DSMC method was originally developed to simulate neutral gases, the simulation software framework applied in this project had to be extended in order to cope with highly rarefied plasma flows. This was done in earlier works by Petkow [26, 14] with contributions from Bozsak [27] and Syring [28].

2.3.2 Plasma interaction model

A high fidelity plasma interaction model is implemented on basis of individual evaluation of interaction probabilities on basis of cross sections. Those are implemented for Argon atoms and its ions considering only electron impact induced processes like ionisation. A full description is available in [26, 14].
The chemical reaction of primary interest is the electron induced ionisation of a ground-state Argon atom following

$$e + Ar \rightarrow 2e + Ar^{+}. \tag{2.18}$$

Here, e is an electron, Ar is the Argon atom and Ar^{+} is the Argon ion. As mentioned before, it is initially evaluated whether a pair of particles do interact. The energy dependent total cross section $\sigma_T(E)$ is calculated as sum over all cross sections possible for the given particle pairing, i.e. in case of $e - Ar$ one gets

$$\sigma_T(E) = \sigma_{ela}(E) + \sigma_{exc}(E) + \sigma_{ion}(E) \tag{2.19}$$

with the subscripts representing *ela*stic scattering, *exc*itation, and ionisation. Knowing σ_T allows immediately to compute the collision probability according to

$$P_c = \frac{\beta_c}{C_{\alpha\beta}} \sigma_T\left(E\right) g \tag{2.20}$$

with

$$\beta_c \propto \frac{N_\alpha N_\beta}{V_{cell}} \Delta t \tag{2.21}$$

being a factor which depends on simulation parameters e.g. particle number N of species α or β in a cell with volume V_{cell} (and thus the density in the cell), and the simulation time step Δt. $C_{\alpha\beta}$ is a characteristic constant for each species pairing and g the already introduced relative velocity between both particles. If $P_c > R$, interaction probabilities P_i are calculated according to

$$P_i = \frac{\sigma_i}{\sigma_T}. \tag{2.22}$$

The probabilistic character of the overall approach is additionally maintained by randomly defining the order in which the possible interaction probabilities are evaluated against R. In case of $n - Ar$ pairing, if neither ionisation, nor excitation occurs despite $P_c > R$, at least an elastic scattering process is performed.

2.3.3 High density model

Typically, each simulated particle represents a relatively high number of physical, i.e. real particles. This number is called particle weight (W). In DSMC, a higher particle weight (or particles discretisation) has impact on statistical aspects like the noise

level in the signal (velocity, temperature). Particle weights can reach 10^{10} and more. However, in PIC the particle weight has a stronger impact on numerical issues like stability. Hence, particle discretisation, at least in the code applied in this study, is limited by the PIC solver and not by DSMC. As will be shown in chapter 5, W should not exceed $10^6 - 10^7$. A brief estimation shows that ate maximum particle weight of $W_{max} = 10^7$ and a neutral particle density $n_{Atom} \approx 10^{21}\,\mathrm{m}^{-3}$ would lead to a neutral's particle number of

$$N_{atom} = \frac{n_{atom}}{W_{max}} V = \frac{n_{atom}}{W_{max}} \left(0.04^3\,\mathrm{m}^3\right) = 6.4 \cdot 10^9 \tag{2.23}$$

in the used simulation region with the Volume V as defined in Sec. 5.1. This number of particles is not treatable in present computational architectures. To avoid this problem, the background gas should be simulated as a continuum instead of a number of particles making use of a Continuum Monte Carlo (CMC) method. Here, only the electrons and ions are modeled as individual particles. The background remains a continuum. For collisional purposes, a neutral gas particle is generated randomly from the Maxwell-Boltzmann distribution for every electron and ion in every time step. So, every electron gets an atom as collision partner in a way most DSMC collision algorithms can be applied without modification. However, having a continuum based background means that advantage can be taken when calculating P_c which is an implicit function of the density. The number of neutral atoms per cell N_{atom} is calculated now as the product of the density n_{gas} and the cell volume V_c: $N_{atom} = n_{gas} V_c$. Thus, β_c becomes

$$\beta_c \propto N_B n_{gas} \Delta t. \tag{2.24}$$

The CMC implementatio is only valid if the number of neutral atoms per cell is much greater then the number of electrons (and ions), i.e.

$$N_{atom} \gg N_{elec},\, N_{ion}. \tag{2.25}$$

In case of IEC, this prerequisite is well fulfilled.

2.4 Introduction to the FP solver

The Fokker Planck solver is based on the theory of the cumulative scattering angle which had been developed by Nanbu [29] with contributions of Bobylev [30]. Here, only a brief introduction will be given, for further details please refer to the given references.

As stated before, Coulomb collisions are associated with scales smaller than the Debye length. If we assume that the PIC solver resolves the plasma according to $x_{cell} \leq \lambda_D$ then we can say that inside each cell the Coulomb collisions are treated without interfering with the states of the neighboring cells. Collision-wise, resolving the Debye length implies $P_c > 1$ for all pairs of charged particles as every charge in the Debye sphere by definition interacts with every other charge in that sphere.

This prohibits a binary treatment modeling. Nanbu found a simple expression for the probability density distribution $F(\chi_N)$ of the cumulative scattering angle χ_N after N scattering processes,

$$F(\chi_N) = 2\pi \sin \chi_N \; f(\chi_N). \tag{2.26}$$

Starting point was the clarification of the coordinate transformation process due to scattering. Given the transformation matrix he simulated N single scattering processes on very small time scales and traced the cumulated scattering angle χ_N. It's distribution as a function of time was approximated quite well by an exponential approach which together with the normalisation condition

$$2\pi \int_0^\pi f(\chi_N) \sin \chi_N \mathsf{d}\chi_N = 1 \tag{2.27}$$

leads to

$$f(\chi_N) = \frac{A}{4\pi \sinh A} \exp\left(A \cos \chi_N\right) \tag{2.28}$$

where A is a function to be defined. Additionally, Nanbu traced the expectation value $\left\langle \sin^2 \frac{\chi_N}{2} \right\rangle$ as a function of N which can be approximated very good by

$$\left\langle \sin^2 \frac{\chi_N}{2} \right\rangle = \frac{1}{2} \left[1 - \exp\left(-\tau\right)\right] \tag{2.29}$$

where τ is still to be defined. The averaging process

$$2\pi \int_0^\pi f(\chi_N) \sin^2 \frac{\chi_N}{2} \sin \chi_N \mathsf{d}\chi_N = \frac{1}{2} \left[1 - \exp\left(-\tau\right)\right] \tag{2.30}$$

in combination with (2.28) allows to identify a relation for the unknown A in Eq. (2.28):

$$\coth A - A^{-1} = \exp\left(-\tau\right). \tag{2.31}$$

System parameters like time step size $\triangle t$, particle densities n, charges q and others are hidden in the so-called isotropy parameter τ:

$$\tau = \frac{\ln \Lambda}{4\pi} \left(\frac{Z_\alpha Z_\beta e^2}{\varepsilon_0 m_r} \right)^2 n_\beta g^{-3} \triangle t. \tag{2.32}$$

Equation (2.31) cannot be solved analytically but numerically. Nanbu [29] provides values for all τ and A which are not covered by the following relation:

$$A = \begin{cases} \tau^{-1} & \text{for } \tau < 0.01, \\ 3e^{-\tau} & \text{for } \tau > 3. \end{cases} \tag{2.33}$$

Figure 2.2 depicts the function $A(\tau)$ on basis of these values. Given that, a sample of χ_N can be obtained from

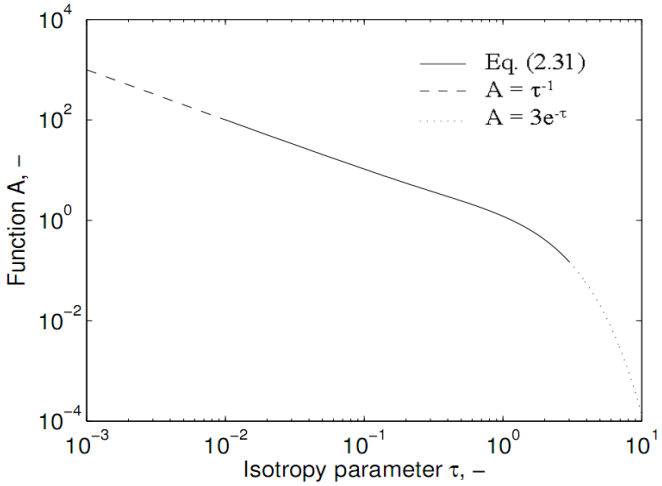

Figure 2.2: A as a function of different τ.

$$\cos\chi_N = A^{-1}\ln\left(e^{-A} + 2R\sinh A\right) \tag{2.34}$$

where the main input parameter is an equally distributed random number $R \in [0,1]$. Once χ_N is known, post-collisional particle velocities (marked with ($'$)) as a result of Coulomb scattering can be derived:

$$\mathbf{v}'_\alpha = \mathbf{v}_\alpha - \frac{m_\beta}{m_\alpha + m_\beta}[\mathbf{g}(1-\cos\chi_N) + \mathbf{h}\sin\chi_N] \tag{2.35}$$

$$\mathbf{v}'_\beta = \mathbf{v}_\beta + \frac{m_\alpha}{m_\alpha + m_\beta}[\mathbf{g}(1-\cos\chi_N) + \mathbf{h}\sin\chi_N]. \tag{2.36}$$

Vector $\mathbf{g} = \mathbf{v}_\alpha - \mathbf{v}_\beta$ represents the pre-collisional relative velocity. In cartesian coordinates one has then

$$h_x = g_\perp\cos\varepsilon \tag{2.37}$$

$$h_y = -(g_x g_y\cos\varepsilon + g g_z\sin\varepsilon)/g_\perp \tag{2.38}$$

$$h_z = -(g_x g_z\cos\varepsilon - g g_y\sin\varepsilon)/g_\perp \tag{2.39}$$

$$g_\perp = (g_y^2 + g_z^2)^{1/2} \tag{2.40}$$

with ε representing the azimuthal (and isotropic) scattering angle.
Verification calculations of this solver based on electron beams shot into an ion and into an electron cloud have been published before, see [26, 14].

3 Assessment of initial particle data

For an adequate simulation, realistic input parameters are needed to initiate the particle interactions and motions. The originally stated problem cannot be treated with the applied kinetic code due to a severe mismatch between the corresponding computational needs and the available resources in this project. Hence, a two staged downsizing of the simulation domain was introduced: Firstly, the overall IEC device was shrinked by a factor of six with respect to the anode diameter. Secondly, only a box covering the inter-electrode jet stream and parts of the plasma core including the cathode's grid opening is simulated, see chapter 4. This simplification procedure imposes the identification of matching inflow particle properties which cannot be derived from literature without further assumptions and scaling laws.
In this chapter, initial particle inflow properties are defined, i.e. particle densities and energies whereas the latter is a superposition of macroscopic velocity and energy distribution (function). Mole fractions are a matter of inflow condition definition and discussed in section 4.

3.1 Reviewed IEC configurations

The publications depicted in table 3.1 for ion and electron density measurements have been reviewed using spherical inertial electrostatic confinement devices and cylindrical electrostatic confinement devices in pulsed and steady-state operation. These references include measurements of averaged electron density or electron density profiles with microwave Fabry-Perot [31, 33] or Laser heterodyne interferom-

Table 3.1: Reviewed reference publications

	Meeker et al. [31]	Dolan [32]	Dobson and Hrbud [33]	Thorson [34]
Shape	cylindrical	cylindrical	spherical	spherical
Plasma generation	electron impact (oxide cathodes)	electron impact (oxide cathodes)	glow discharge	electron impact (tungsten filaments)
Propellant	Deuterium	Neon	Argon / Deuterium	Hydrogen
Grids	2	2	2	3

etry [31, 32] and also electrostatic probe measurements [34] within the cathode grid. A database has been established from all this data. Given that the IEC setup at IRS (see chapter 1) is based on two spherical electrodes with a steady-state Argon based glow discharge, the data published by Dobson and Hrbud [33] was selected as reference configuration although the data is still incomplete. This decision was additionally motivated by the fact that the data set, incomplete though, is the largest compared with the other data sets and personal contacts to the authors (for communication and clarification purposes) exist.

3.2 Reference operation condition

Four different test conditions have been studied in [33] with 2 x Argon and 2 x Deuterium. The major difference between both Argon conditions where the cathode voltages $V_c = -1040V$ and $V_c = -1010V$. The condition related to the second cathode voltage (with additional parameters listed in table 3.2) was selected as reference since this value is very close to the electrode voltage of the IRS design ($-1kV$). The difference of 1% is covered by the uncertainty of the voltage supply and of the measurement techniques.

Table 3.2: Setup and Argon operation conditions taken from Dobson & Hrbud: Cathode voltage V_c, anode voltage V_a (grounded), power supply current I_{PS}, anode diameter d_a, cathode diameter d_c, chamber volume V_{ch}, chamber pressure p_{ch}

$V_c\ [V]$	$V_a\ [V]$	$I_{PS}\ [mA]$	$d_a\ [m]$	$d_c\ [m]$	$V_{ch}\ [m^3]$	$p_{ch}\ [mbar]$
-1010	0	50	0.6	0.23	0.905	$2.67 \cdot 10^{-2}$

3.3 Species densities

Dobson and Hrbud [33] performed vast measurement campaigns, partly for the identification of electron densities in the IEC plasma cores. These values were used with a simplified numerical scheme to identify also particle densities of ions.

3.3.1 Electrons and ions

Electron density measurements via microwave interferometry show transverse profiles that are generally flat (no peaks). In some cases, the profiles have eccentric symmetric minima yielding mean electron densities from $0.4 - 7 \cdot 10^{16} m^{-3}$. Numerical solutions of a one-dimensional Poisson equation for IEC plasmas were reviewed and energy distribution functions were identified which give flat transverse profiles. These

functions were used with a plasma approximation to obtain solutions which also give densities consistent with the measurements, see table 3.3. The measured electron particle density is close to the numerically obtained value.
In the simulations performed in this study, numerically derived electron particle densities were used for the sake of consistency.

3.3.2 Neutrals

Given a known background chamber pressure p_{ch}, the neutral's particle density can be obtained via the ideal gas equation of state

$$p_{ch} = n_n k_B T_n. \tag{3.1}$$

The temperature T_n was not measured, hence Dobson and Hrbud provide a crude estimation leading to $T_n = 1000K$ as a consequence of microwave heating during the measurements. An exemplary variation of $300K < T_n < 1000K$ does not change the order of magnitude of n_n such that calculation is performed with $T_n = 1000K$ yielding $n_n = 1.93 \times 10^{20} m^{-3}$.

Table 3.3: Core particle densities in 10^{16} $[m^{-3}]$, taken from Dobson & Hrbud

	$n_{e,c}$	$n_{i,c}$	n_n
Experiment	2.6		
Num. model	4.031	4.04	1.93×10^4

3.4 Species temperatures

Due to the novelty associated with the IEC jet extraction research, a full data set, i.e. experimental data of plasma jet properties jointly published with IEC plasma core properties and geometric dimensions leading to jet extraction, does not exist. Accordingly, published data of particle densities and temperatures for the same setup do not exist. Theoretical considerations derived from the plasma source were used to estimate an order of magnitude of the particle temperatures.

3.4.1 Ions

The applied plasma source for the experiments conducted in [33] produced a glow discharge. Typically, a glow discharge is in thermal non-equilibrium with $T_i \approx 300K$ [35]. Other sources of ions are not considered due to lack of data.

3.4.2 Primary electrons

Generally, at least two populations of electrons are distinguished in IEC devices depending on their origin of birth. Within a glow discharge the so called primary electrons are created, a temperature T_e of $10000K$ is not unusual for this type of electron generation [35].

3.4.3 Secondary electrons

It is known (see e.g. [31]) that the inner electrode has a secondary source of electrons with a different energy distribution than the primary electrons. However, it is not clear yet which physical phenomenon is responsible for secondary electron generation, hence different possibilities are considered here:

- *Field Emission*: The Fowler-Nordheim equation [36] is elaborated, yielding an electron current density due to a tunneling effect:

$$j(E) = \frac{q^3 m^*}{8\pi h m W_e} E^2 \exp\left(-\frac{8\pi\sqrt{2mW_e^3}}{3qhE}\right) \tag{3.2}$$

  Field emission occurs when a strong electric field E enables electrons, bound in a solid, to tunnel through the barrier and escape the solid. In Eq. (3.2), q, m^*, m, W_e, and h represent the charge of the tunneling particle, the effective mass of the tunneling particle [37], the particle's mass in the dielectric, the work function, and Planck's constant. With $W_e = 7.0488 \times 10^{-19} J$, $m^*/m = 8$, and $E = U/d = 1kV/0.185m = 5405.1V/m$ this yields a vanishing current density j. A closer look at Eq. (3.2) shows that the reason for a vanishing field emission contribution originates in the exponential term. The electric field has been derived from $E = U/d$ yielding electric fields which are significantly lower than what should be expected in reality. However, due to problems related to mesh generation close to the electrode's wires it was not possible to derive a more precise information from the OpenFOAM calculations described in section 4.2. We conclude that field emission still might play a role for two reasons:

  1. The electric field lines close to the grid wires are deformed in a way that field line densities are increased close to the electrode's wires.
  2. The wire's surface is not perfect. In best case, surface roughness is the only cause of a huge number of very tiny electric field line concentrations. Due to the geometrical properties of the individual tiny material accumulations on the surface the effective electric field is increased such that the estimated field emission might become non-vanishing and even significant.

  Future works should focus on both points, in this study we assume field emission generated electrons to be negligible.

- *Thermionic Emission*: The effect of thermionic emission is estimated at the cathode using the Richardson-Dushman equation:

$$j(T) = A_R T^2 \exp\left(-\frac{W_e}{k_B T}\right) \tag{3.3}$$

Here, j is the emitted current density of the cathode (in consequence of the thermionic emission), T is the temperature, k_B is the Boltzmann constant, and A_R is the Richardson constant which was estimated by Dushman [38] according to

$$A_R = \frac{4\pi m_e k_B^2 e}{h^3} = 1.20173 \times 10^6 \frac{A}{m^2 K^2}. \tag{3.4}$$

This value of A_R is an upper limit of the thermionic emission. Suppose that the cathode is made of stainless steel, then the work function is $W_e = 4.4eV$ [38]. If the cathode has a temperature of $T_c = 500K$, then the resulting current density equals $j = 1.34 \times 10^{-33} A/m^2$. The connection between the current density and the charge is given by $jA = Q/t$. For the wire surface area of $A = 0.00834m^2$ and an estimated simulation time of $t = 1ns$, the charge is $Q = 1.12 \times 10^{-44} C$. Given that, the number N_e of emitted electrons during the simulation time t leads to $n_e = Q/e \approx 7 \times 10^{-26} = 0$.

Next, the Schottky effect [39] is considered as it reduces the work function according to

$$\Delta W_e = \sqrt{\frac{e^3 E}{4\pi\epsilon_0}}. \tag{3.5}$$

Given the numbers introduced before it follows that $\Delta W_e = 0.0028eV$. Now, the corrected current density is $j_{Schottky} = 1.43 \times 10^{-33} A/m^2$ which leads to a small theoretical number of emitted electrons during $1ns$ of $N_e = 7.44 \times 10^{-26} = 0$. Hence, the effects of the thermionic emission are neglected in this study.

- *Ion-Grid Collisions*: Some positive ions that are accelerated, might be able to unhinge electrons from the grid surface by impact if their energy exceeds the work function. But the part of kinetic energy that is transferred to the grid is mostly thermal energy and just a low percentage accounts for electron emission [40].

- *Neutral - Neutral Collisions*: Ionisation processes due to reactive collisions between neutrals are expected to occur only after a charge exchange process leading to a high energy neutral (and a low energy ion). Therefore, this source of electrons is considered as negligible.

- *Neutral - Ion Collisions*: Initial discharge ions produced between the electrodes are accelerated towards the cathode. The acceleration distance varies depending on each ion's birth place. Hence, the maximum ion velocity is reached at r_c after a steady acceleration over a maximum distance of $r_a - r_c$. Other acceleration effects inside the cathode are neglected here for the sake of simplicity. The expected ion energies are considered to be low ($\sim keV$). Hence, cross sections taken from [41] were analysed for the $Ar^+ - Ar$ case. With $U = 1kV$ and assuming a constant radial field acceleration we get $\sigma_{ion} \sim 10^{-18}m^2$ which is surprisingly large. However, the authors of Mittleman and Wilets [41] also criticise the poor number of cross section data points and the mismatch between the measurement and the theory applied to derive the cross section fit model. However, the agreement between the data points and the fit curve(s) is very good and the qualitative difference between different species and a model parameter interpreted as the sum of radii of each considered ion species (He^+, Ne^+, Ar^+) is correctly represented. Unfortunately, the considered energy range is outside the energy range of the experimentally obtained cross sections data points which induces additional uncertainty in the cross section information. Future research activities should clarify whether this ionisation process can serve also quantitatively as electron source inside the plasma core.

- *Ion - Ion Collisions*: Given the high number of ionisation levels of Argon the reaction $Ar^+ + Ar^+ \rightarrow Ar^{2+} + Ar^+ + e$ as a potential electron source inside the cathode might play a role. However, reliable cross section data could not be identified. On the other hand, the second ionisation energy is significantly higher than the first one such that it is assumed that this process is neglected.

All assumptions introduced here should be verified in further studies as this is outside the scope of this ARIADNA project. In all simulations, electrons have been initialised with $T_e = 1300K$. Despite the fact that this number is not justified by reference or own concrete estimations, a sensitivity analysis has shown negligible difference in the results compared to $T_e = 10000K$. The latter is an upper limit estimation keeping in mind the different sources (primary vs. secondary electrons). The low impact of the choice of initial electron temperature is due to the impact of the electric field on electron energy with respect to thermal movement. Hence, assuming $T_e = 1300K$ is considered an acceptable estimation.

3.4.4 Neutrals

As stated in section 3.3, the neutral particle's temperature was crudely estimated to be $T_n = 1000K$ in [33]. This assumption is based on the fact that high power microwave interferometry was used to investigate the electron density distribution and the corresponding radiation most probably heated up the neutral gas. In the simulation setup heating radiation does not occur. Hence, the neutral particle's temperature was assumed to be $T_n = 300K$ which is also supported by e.g. [35].

3.5 Species Velocities

Since only the jet extraction shall be simulated the ion acceleration process caused by the external field between the grids has to be considered in a way that ions have a predefined velocity when inserted into the simulation region.

3.5.1 Ions

The acceleration of ions from anode to the cathode can be estimated assuming a planar electrode configuration. The initial radial ion velocity component equals then

$$v_i = \sqrt{\frac{2q_i V_c}{m_i}} \tag{3.6}$$

with the particle charge q_i, cathode voltage V_c (assuming the anode is grounded) and ion mass m_i. After a couple of passes through the plasma core including elastic scattering with other particles, the accelerated ions are lost to either the grid or to so-called charge exchange reactions with their neutral counterparts. A quantification of this highly dynamic process is currently impossible such that the average macroscopic velocity ($\mathbf{v}_i = 0$) of these ion oscillations are applied during initialisation. Acceleration processes depend solely on external electric fields as well as on inter-particle interactions provided by the PIC solver.

3.5.2 Electrons and Neutrals

Electrons drifting outside the cathode are neglected. Neutrals are assumed to remain basically static between the electrodes so their velocities are neglected as well.

4 Assessment of initial geometry data

This chapter summarises the activities and decisions made leading to the final simulation domain. Due to the high accuracy of the Maxwell solver the initially identified reference geometry was down scaled twice. First, the grid dimensions were reduced by a factor of six according to the anode's diameter, see Sec. 4.1. The Maxwell solver's output is reduced to the electric and magnetic fields generated by the charges in the plasma while the external electric field is provided by a proper tool as described in Sec. 4.2. Second down scaling of the simulation domain is described in Sec. 4.3.

4.1 Reference simulation setup

As mentioned previously, literature does not provide a proper reference by means of a sufficiently studied IEC plasma configuration including grid openings leading to a jet extraction.
Therefore, the following procedure was developed: Meyer [42] provides geometric grid information but no reliable plasma properties unlike Dobson and Hrbud [33] which provide useful plasma data but measured in a standard IEC configuration (w/o grid openings). Since the detailed grid with its wires and spacings is not included in the simulation grid (see Sec. 4.2) the ratio of grid spacing to grid opening for the jet will not have an impact, but the ratio of the jet grid opening in cathode grid $d_{c,O}$ to jet grid opening in anode grid $d_{a,O}$ will, see Fig. 4.1. Assuming that the grid openings scale according to Meyer [42], hypothetical grid openings can be devised for the IEC configuration of Dobson and Hrbud [33] which is then scaled down by a factor of six with respect to the anode's diameter d_a in order to reduce computational load, see Tab. 4.1. Of course, this method implies the assumption that neither the scaling of the grid

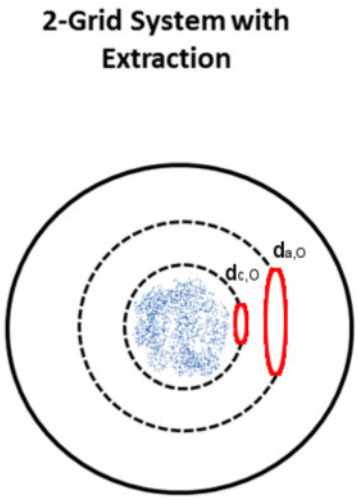

Figure 4.1: IEC setup with grid openings.

openings nor the down scaling of the whole IEC setup affects the measured plasma properties identified in Dobson and Hrbud [33].

Table 4.1: Reference grids and simulation setup.

	Meyer [42]	Dobson and Hrbud [33]	Simulation Setup
d_a	$0.457m$	$0.6m$	$0.10m$
d_c	$0.095m$	$0.23m$	$0.034m$
$d_{a,O}$	$0.142m$		$0.024m$
$d_{c,O}$	$0.04m$		$0.0066m$

4.2 Electrostatic background field calculation

In general, the total electric field $\mathbf{E}$ which is seen by a charge is a superposition of the local electric background field and the field caused by all other charges in the computational domain. In case of the IEC, potential boundary conditions are required, i.e. it is necessary to define a voltage on the acceleration grids to obtain the electric background field according to

$$\mathbf{E} = -\nabla\phi. \tag{4.1}$$

However, the transient Maxwell solver described in section 2.2 algorithmically does not allow to incorporate a potential boundary condition, only E_i or $\partial_{x_i} E_i$ for $i = 1, 2, 3$ is possible. To circumvent this problem the electric field calculation is separated into the calculation of the background field $\mathbf{E}_{bg}$ and the electric field $\mathbf{E}_{in}$ induced by the charges in the plasma. Once both values are known throughout the domain (i.e. on all grid points), they are superimposed. This procedure implies that the plasma does not affect the boundary conditions due to the constantly applied grid voltage. Hence, $\mathbf{E}_{bg}$ is calculated once in the beginning of the simulation and remains constant.
The electrostatic background field is generally obtained by solving the Laplace equation

$$\Delta\phi = 0 \tag{4.2}$$

for given boundary conditions (applied voltage, e.g. $-1kV$) while no charged particles are inside the simulation domain. Technically, an external open source based solver (OpenFOAM - *electrostaticfoam*) is used. The work flow for the calculation of Eq. (4.2) can be described as follows:

- use OpenFOAM to solve Eq. (4.2) with potential boundary conditions,
- converting the solution into VTK format (Visualisation Toolkit),

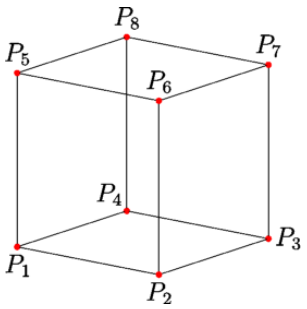

Figure 4.2: Example of a hexahedral cell.

- load VTK file into the particle solver, and
- transfer of the background field to the particles via interpolation.

The interpolation of the field data from the mesh to the particles is performed in the following way: For every node of a hexahedral element (see Fig. 4.2) a value for $\mathbf{E}_k = [E_x, E_y, E_z]$, for $k = 1, 8$ is stored. A particle located at $\mathbf{x}_i = [x_i, y_i, z_i]$ in the element is affected by the background field $\mathbf{E}_i$ according to

$$\mathbf{E}_i = \frac{\sum_{k=1}^{8} \sqrt{|\mathbf{x}_i - \mathbf{P}_k|}\mathbf{E}_k}{\sum_{k=1}^{8} \sqrt{|\mathbf{x}_i - \mathbf{P}_k|}}. \tag{4.3}$$

This procedure is comparable to a volume-weighting in case of a Cartesian grid.

The original IEC grid geometry is a huge challenge for mesh generators. The spherically arranged small wires lead to a huge number of small mesh cells close to the wires' surface. This is impracticable for most mesh generators and only processable in a huge amount of time. Therefore, we use two spherical shells with respectively one hole for the jet extraction as geometry, see Fig. 4.3. The complete OpenFOAM mesh has 65600 hexahedral cells.
The only significant difference of the electric field between this geometry and the original IEC geometry will be close to the sphere shells. But the non-symmetric $\mathbf{E}$ field which affects the particle motion should be comparable since the focus is on the jet extraction. The boundary conditions for the OpenFOAM simulation are:

- Outer sphere with geometry data listed in Tab. 4.1 and the potential $V_a = 0V$,
- Inner sphere with geometry data listed in Tab. 4.1 and the potential $V_c = -1kV$,
- Volume is defined as vacuum in a box with the edges $0.12 \times 0.12 \times 0.12m$.

The results of the OpenFOAM simulation are shown in Fig. 4.4. The results are as expected. The electric potential is approximately constant inside the inner sphere and outside the outer sphere. Accordingly. the electric fields are very small there. Figure

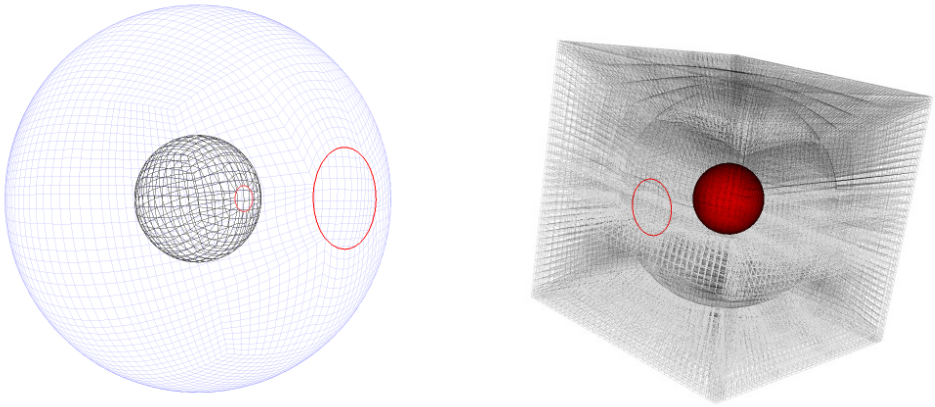

Figure 4.3: Left: Surface mesh of the two spherical shells with the holes (red). Right: The whole simulation mesh with depicted cell structures, the inner sphere, and the hole of the outer sphere (red).

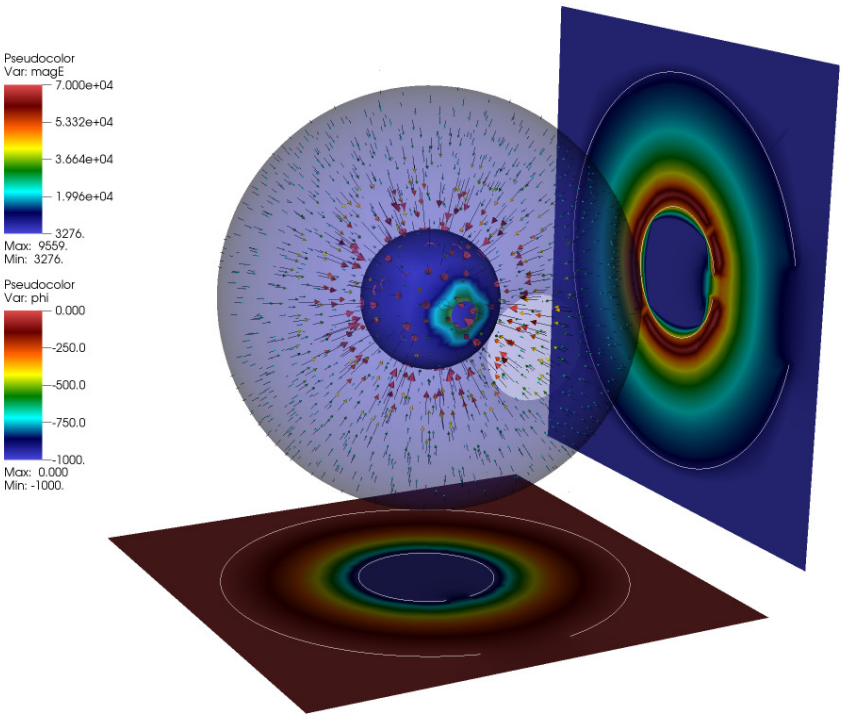

Figure 4.4: The arrows show the electric field vectors, their colors and lengths are scaled by the electric field's magnitude. Slices through the center showing the magnitudes of the electric field (right) and of the electric potential (bottom).

4.5 shows that the electric field in the inner sphere does not vanish completely. This is important for the jet extraction of the particles. Especially the streamline plot of the electric field vectors, starting in the inner sphere, is interesting. The plot provides information about the hypothetical (i.e. non-disturbed by other phenomena) stream path of particles accelerated in the inner sphere by the external electric fields.

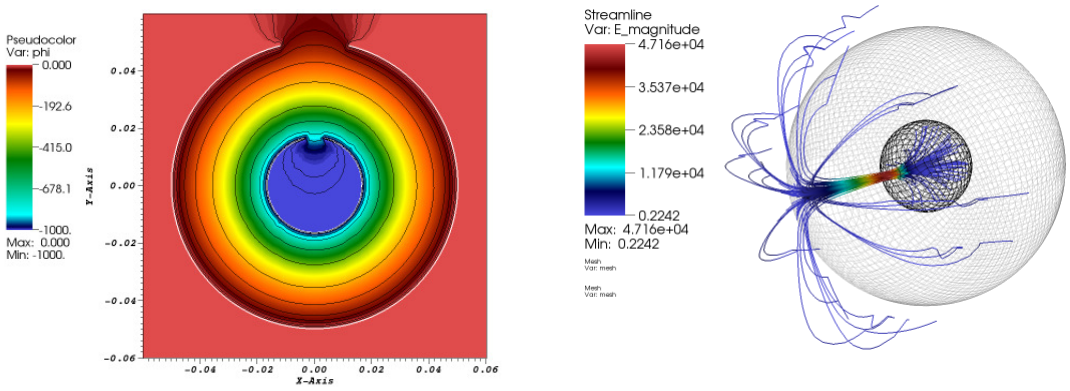

Figure 4.5: Left: A slice through the center of the magnitude of the electric potential with equipotential lines and a skewed data scale (color table) to show the small variations of the electric potential in the inner sphere and outside the outer sphere. Right: A stream line plot of the electric field vectors that starts in the inner sphere.

4.3 Final simulation domain

The whole two grid system will not be simulated due to the respective computational needs. Therefore, a smaller simulation domain covering the jet extraction volume is considered, see Fig. 4.6. A new hexahedral grid was defined for this region.
The solution of the OpenFOAM solver was then transferred from the original mesh to the new but smaller mesh. For this purpose, a tool was developed that cuts out a subregion of the OpenFOAM solution and interpolates the electric field values from the nodes of the old mesh to the nodes of the new mesh. The interpolation is realised similarly to Eq. (4.3) where the particle positions correspond now to the new mesh's nodes. The work flow is shown in Fig 4.7.
The new hexahedral mesh with the symmetrically structured cells reduces the computational demand further. The smaller and the more warped the cells are (as in the original OpenFOAM mesh close to the sphere shells and the holes), the smaller is the global time step for a stable Maxwell solution. With the original mesh, a maximum time step of about $10^{-16}s$ is necessary for a stable Maxwell solution. The new mesh allows a time step of about $10^{-12}s$.

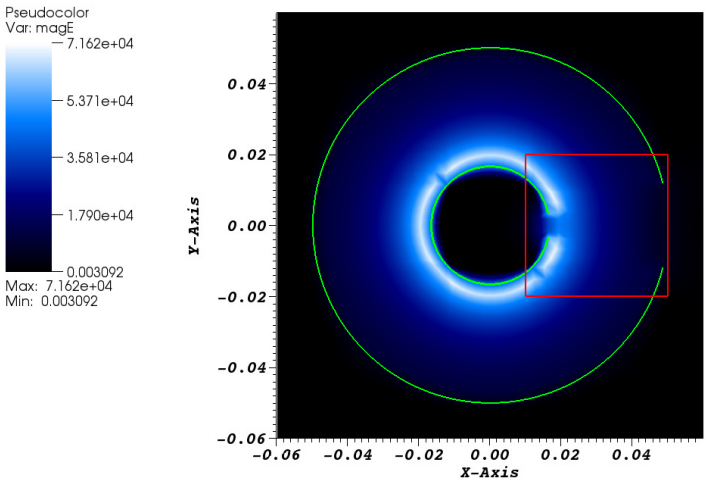

Figure 4.6: Magnitude of the electric field with the original spherical geometry (green) and the final simulation domain (red).

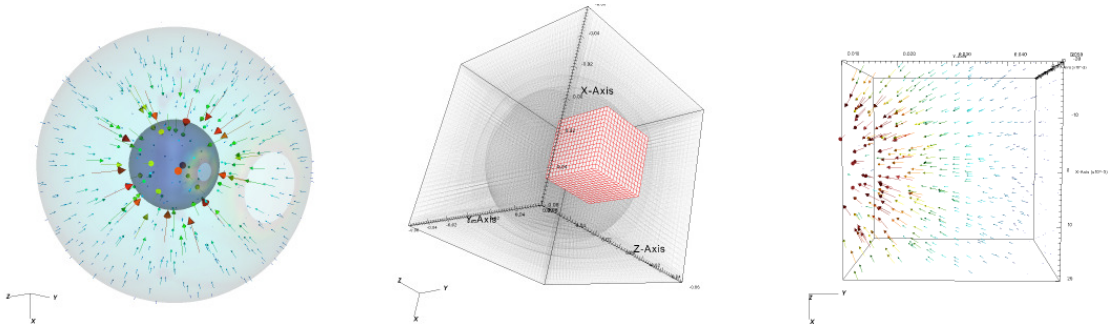

Figure 4.7: Left: Original electric field vectors with the two IEC spheres. Middle: New simulation mesh (red) on the corresponding position in the old original mesh (black with opacity). Right: New electric field vectors cutted from the original mesh.

5 Preparatory Simulations

Several preparatory simulations were performed in order to quantify numerical key parameters suitable for the IEC configuration. The temporal discretisation is defined by the PIC solver and the smallest cell in the simulation domain. However, spatial and particle discretisation cannot be deduced without preparatory simulations. Also, estimating the need for shape functions and chemical reactions demands costly preparatory work. These four aspects will be addressed in this chapter.

5.1 Spatial Discretisation

A typical measure for the estimation of the necessary cell sizes to obtain mesh-independent results in a PIC simulation [18] is the Debye length. In case of an IEC device with a typical ion temperature of $T_i = 300K$ and ion particle density of $n_i = 10^{16}m^{-3}$ one gets $\lambda_D = 1.1 \cdot 10^{-5}m$. A box like simulation domain with side lenghts of $\approx 0.037m$ the obtained λ_D leads to 3700 cells in each direction. The computational costs related to a total of $\approx 5 \cdot 10^{10}$ cells are unfeasible. Therefore it is not advisable to resolve the Debye length here. Contrarily, it is known that a crude under-resolution in combination with other numerical parameters might negatively impact on numerical stability and energy conservation such that a grid resolution needs to be identified which leads to a stable solution and where further refinement does not change the solution. Such an analysis is performed in this section and the resulting mesh will be applied to the final simulations presented in chapter 6.

5.1.1 Simulation setup

For this preparatory simulation, the used simulation domain equals the final simulation domain presented in Sec. 4.3. Particles of each species can leave the domain via the boundary faces. The simulations discussed here were all done with a polynomial degree of $n = 2$, a particle weight of $W = 10^5$, and a temperature of $T_i = T_e = 1300K$. Further, the ion particle density $n_i = 8{\cdot}10^{16}m^{-3}$ is used to uniformly distribute all ions in the domain. The applied electron particle density n_e equals also $8 \cdot 10^{16}m^{-3}$. However, the electrons are inserted only in a small box of $V_{Box} = 0.028 \times 0.028 \times 6.248 \cdot 10^{-8}\,\mathrm{m}^3$ at the left-hand side of the mesh, see Fig. 5.1. The inflow rate is such that the overall charge density in the box is set to equal $n_i = n_e$. Both ions and electrons are inserted without initial flow velocity (but with thermal components) which mimics an ”electron reservoir” state inside the inner electrode of the IEC. The resulting electron motion is

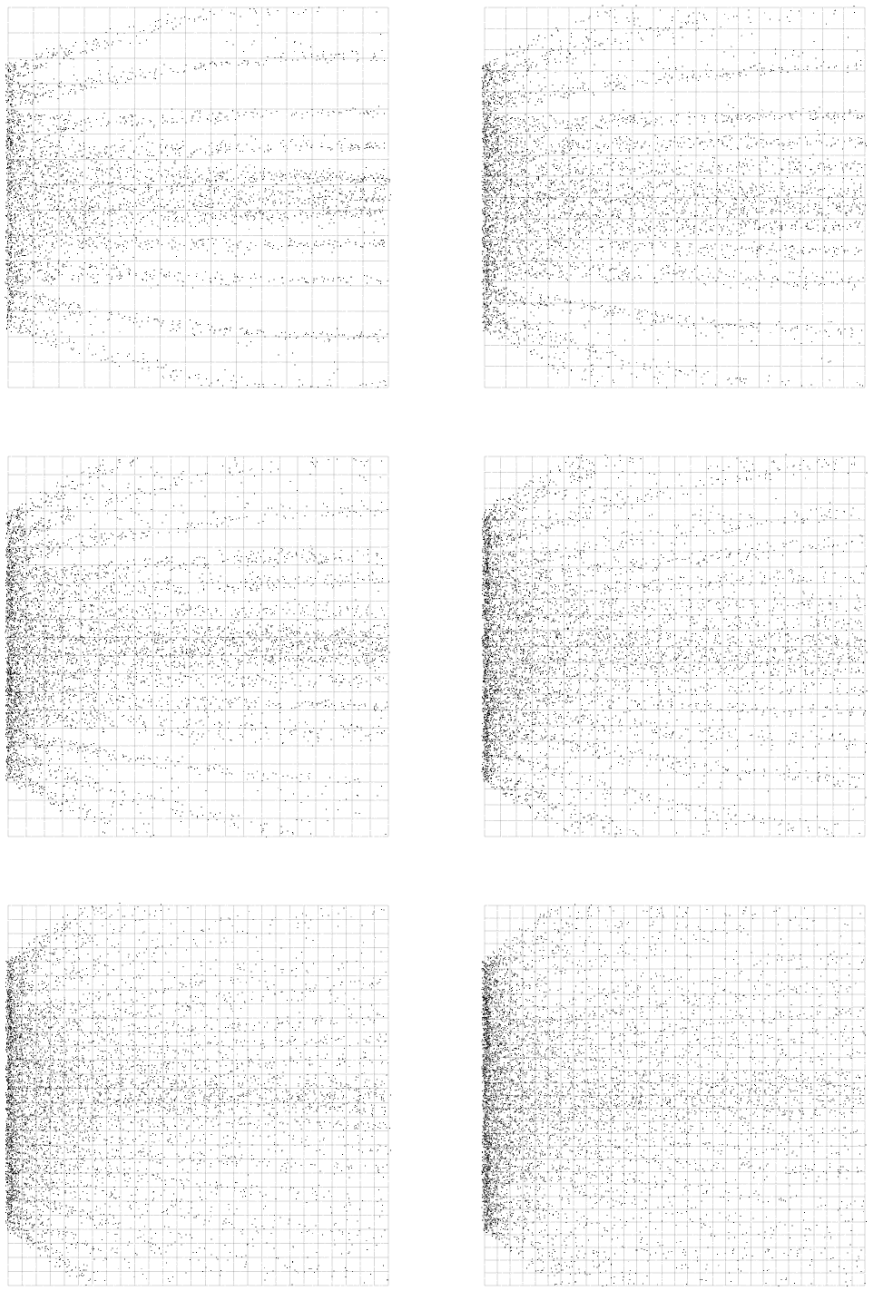

Figure 5.1: Electron distribution on different meshes after $8ns$. Only the electrons are shown because the ions practically do not move during this short period. TL: 3375 cells, TR: 5832 cells, CL: 9261 cells CR: 13824 cells, BL: 19683 cells, BR: 28000 cells.

only a consequence of the interactions between self-fields of electrons and ions and the externally applied electric fields.

5.1.2 Results

Figure 5.1 shows the different results with the different meshes after the same simulation time $8ns$. A grid independent solution is obtained if there are no significant changes in the results after further mesh refinement and when mesh artefacts (like the non-physical particle jets in Fig. 5.1, Top Left picture with 3375 cells) are no longer visible. The mesh with 19683 (Bottom Left) cells was finally selected to serve as simulation mesh due to converging results and a reasonable number of cells. In that mesh, the ratio of cell length to Debye length yields $\lambda_{cell}/\lambda_D \approx 170$.

5.2 Particle Discretisation

Particle discretisation is expressed via the particle weight W which is the number of real particles represented by one simulated particle, i.e. $N_{real} = WN_{sim}$. This discretisation affects both the particle mass as well as the particle charge. Hence, the Lorentz force per particle scales with W according to

$$\mathbf{F_{Lor}} = Wq\left(\mathbf{E} + \mathbf{v} \times \mathbf{B}\right) = Wm\mathbf{a}. \tag{5.1}$$

A change in particle discretisation does not affect particle acceleration $\mathbf{a}$. Nevertheless, particle discretisation does have an impact on particle behavior in several other ways:

- The smaller W the more particles are in the system such that distribution functions are better represented.
- The smaller W the less necessary is the application of shape functions which improve numerical stability and energy conservation in PIC codes. This will be discussed in section 5.3.

In this section, the quality of the representation of a velocity distribution function in one direction has been selected as criterion. With a plasma initially at rest, the velocity distribution function in one direction using $T_e = 1300K$ looks as depicted in Fig. 5.2. An external one-dimensional electric field is applied and the impact of W on the distribution function's representation of moving electrons is studied under stepwise reduction of W until no significant impact of W on the solution is recognised.

5.2.1 Simulation setup

The mesh is the same as described in Sec. 5.1 but with all particles (i.e. only electrons) initially at rest and distributed throughout the domain. Apart from the variation

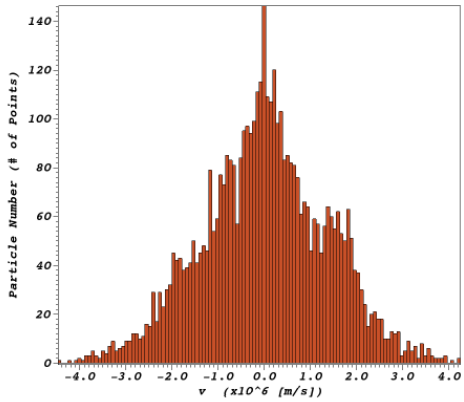

Figure 5.2: Gaussian velocity distribution function (exemplarily measured in x direction) of electrons at rest with $T_e = 1300K$.

of W, the only additional difference is the application of a simple external electric field according to $\mathbf{E} = (0, E_y, 0)^T$ with $E_y = -6.284 \cdot 10^4 V/m$. This value is chosen in reference to the magnitude of the OpenFOAM solution (measured in the middle between both electrodes at the backside of the enhanced grid openings), see Sec. 4.2. The field should accelerate the electrons into y direction leading to a known velocity distribution function in y direction - a shifted Gaussian.

5.2.2 Results

The results are graphically summarised in Fig. 5.3. Particle discretisation is varied according to $10^5 \leq W \leq 10^7$. Simulations with $W = 10^5$ are defined as reference results in order to simplify comparison and visualised as grey background blocks. The left diagram contains two curves, one in brown and one in orange. The right diagram compares a green, a red, and a blue curve with the reference. Clearly, the higher W, the worse the distribution function's discretisation. The brown curve ($W = 2 \cdot 10^5$) provides a good match. Also so for the orange curve ($W = 5 \cdot 10^5$) although there is already first significant deviation in the peak region. Statistics are getting worse with increasing W as observable in the right diagram. Experience shows that $W > 10^6$ leads to non-physical effects and instabilities in the applied PIC solver. The largest deviation from the reference happens with $W = 10^7$ (blue curve). Due to these results particle weights between $10^5 < W < 5 \cdot 10^5$ are used for the following simulations. Whenever possible $W = 10^5$ but W never exceeds $5 \cdot 10^5$.

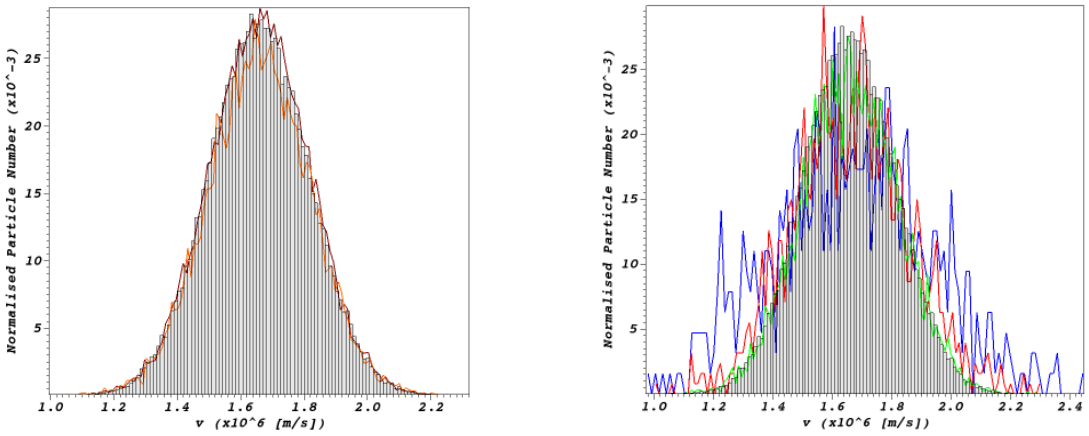

Figure 5.3: Gaussian electron velocity distribution function shifted into y direction. Grey background blocks: reference values obtained with $W = 10^5$. Left: brown ($W = 2 \cdot 10^5$) and orange curve ($W = 5 \cdot 10^5$). Right: green ($W = 10^6$), red ($W = 5 \cdot 10^6$), and blue curve ($W = 10^7$).

5.3 Shape Functions

The applied PIC solver covers long range charge interactions across grid cells by solving the full set of Maxwell equations, see Sec. 2.2. Therefore, the charges need to be assigned to one or several characteristic cell points, hereafter called grid nodes. Different ways to realise this exist - from *Nearest Grid Point* where each charge is fully assigned to the closest grid point, to sophisticated shape functions which mimic a pre-defined spatial charge distribution of each charge, making each of them visible to multiple grid nodes. The latter improves physical representation by reducing the impact of particle discretisation and, correspondingly, numerical stability properties. However, those algorithms are costly and usage is recommended only if necessary.

5.3.1 Simulation setup

The very same configuration as described in Sec. 5.1 is used for identifying the necessity of shape functions in the final IEC simulations. To study the impact of n_e, two different electron densities $n_{e1} = 6.12 \cdot 10^{15} m^{-3}$ and $n_{e2} = 8.16 \cdot 10^{16} m^{-3}$ are applied, each one with and without shape functions. Initially, velocity vectors are compared visually. More accurate information is obtained by observing the electron's velocity distribution functions in y direction which is the direction of acceleration (also on basis of the externally applied electric field as described in previous sections). A major disturbance of the velocity distribution is expected which allows comparison.

5.3.2 Results

Figure 5.4 shows velocity vectors on basis of n_{e1} with (left) and without (right) shape functions [22]. No relevant differences are observable in Fig. 5.4. The results for n_{e2} are very similar such that they are omitted here.

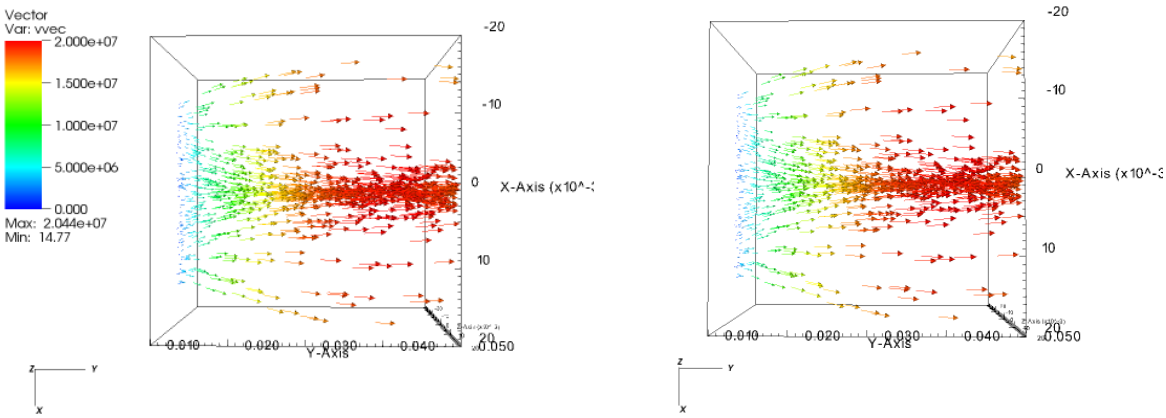

Figure 5.4: Velocity vectors of electrons with the density $n_{e1} = 6.12 \cdot 10^{15} m^{-3}$ with (left) and without (right) shape functions.

The results in Fig. 5.5 show no relevant differences between the simulations with and without shape functions for both densities. Therefore, the final IEC simulations are performed without shape functions to reduce the numerical effort.

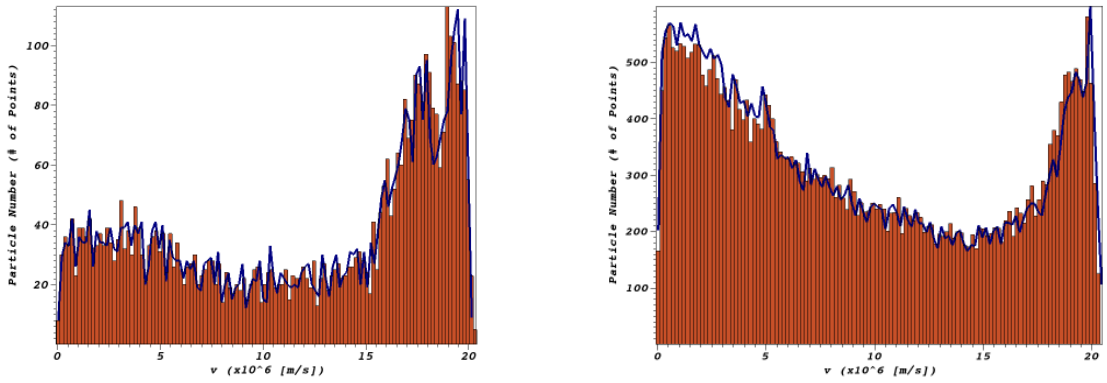

Figure 5.5: Gaussian distribution of the velocity in y direction of electrons with a temperature of $T_e = 1300\,\mathrm{K}$. The orange blocks are the result with shape function and the blue line is the result without shape function. Left $n_{e1} = 6.12 \cdot 10^{15} m^{-3}$, right $n_{e2} = 8.16 \cdot 10^{16} m^{-3}$.

5.4 High density model CMC

Binary short range collisions are performed via the DSMC method. A modification has been implemented in order to cope better with high density problems as DSMC is best suited for low density problems. However, the high density CMC model works reliably only under certain conditions which are verified in this section. The simulation setup of the previous preparatory simulations is not applicable to DSMC. Hence, a more generalised configuration is used which still allows to draw conclusions in terms of the model's applicability to the stated IEC problem.

5.4.1 Simulation setup

As introduced in Sec. 2.3.3, the high density model demands a slight modification of the collision probability computation. In DSMC, P_c depends partly on the number of simulated particles in the cell. However, in CMC this dependence is related to the background particle density which usually (and in the case here) does not vary over space. A non-dimensional box is initially filled with 50 electrons and with a neutral background gas at different densities (see Fig. 5.6). A homogeneous electric field ($E = 2 \cdot 10^6 V/m$) accelerates the electrons to higher energies leading to different electron-atom collision probabilities over time. These P_c values are ensemble-averaged at each time step and put in comparison with DSMC based results.

5.4.2 Results

Figure 5.6 shows the temporal evolution of the ensemble-averaged $\bar{P}_c$ for three different neutral gas densities n. In all three cases the CMC results compare very well with the DSMC results. The simulations have been repeated under variation of n_e/n in order to verify the validity of the $N_{atom} \gg N_{elec}$ condition as well as its limitations. The results are shown in Fig. 5.7. The points are the maximal relative difference of $\bar{P}_c$ for the DSMC and the CMC method. The difference in the region of $n_e/n \lessapprox 10^{-4}$ is nearly zero. In the case this very small difference here is a consequence of the statistical noise in the DSMC method caused by the low electron numbers. The difference will become zero if the averaging time will be longer in DSMC. From a ratio of $n_e/n > 10^{-4}$ the difference between the methods becomes significant and increases almost exponentially.

The course of the graph at $n_e/n > 10^{-4}$ corresponds to the expectations because of the increasing impact of phenomena which should not be neglected. This concerns the momentum transfer between neutrals as well as electron-electron collisions. Thus, the gradient of the graph will depend on the respective physical case (density, electric field, spatial particle distribution). According to these preparatory simulations the particle density ratio n_e/n should always be $\lessapprox 10^{-4}$ in order to be on the safe side if CMC is used instead of DSMC. This is the case for all planned simulations described in the subsequently following chapter. In fact, all simulations including short

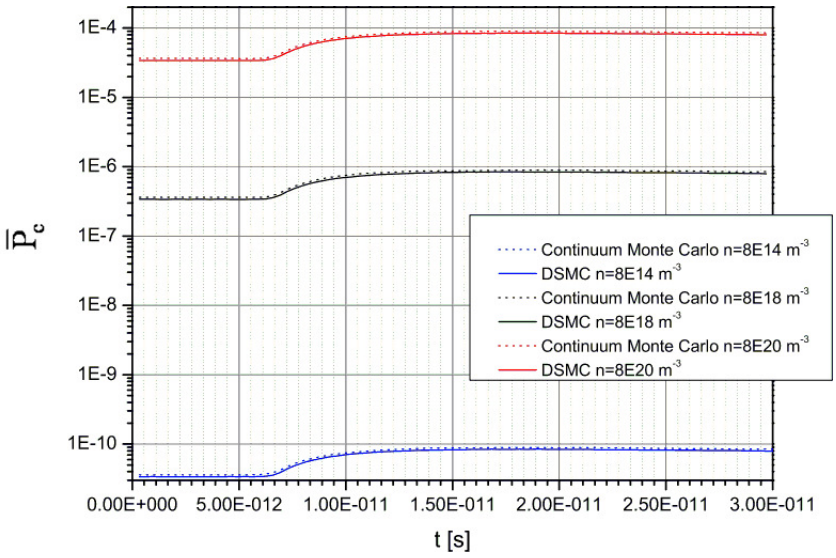

Figure 5.6: Evolution of ensemble-averaged collision probability $\bar{P}_c$ over time for 50 accelerated electrons in three background densities n.

range interactions are simulated with CMC instead of DSMC in order to make the simulations computationally feasible.

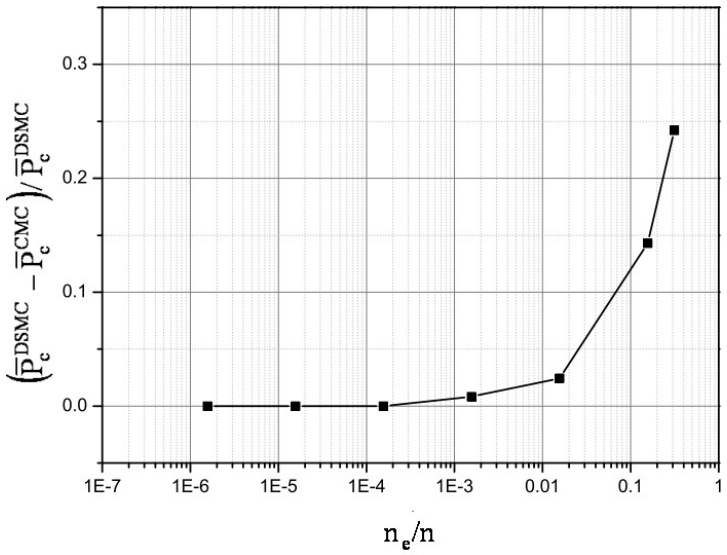

Figure 5.7: Maximum relative difference of $\bar{P}_c$ at different ratios of n_e/n.

6 Main Simulation Results

This chapter presents a summary of the main simulation results aiming at resolving the underlying jet extraction mechanisms in an IEC device in jet mode. Three parameter configurations are studied driven by the circumstance that down-sizing imposes the necessity to define proper inflow and boundary conditions which would not be necessary in case of a full-domain simulation. An overview is given in Tab. 6.1. In jet simulation 1 which is described in Sec. 6.1 it is assumed that Argon ions are initially uniformly distributed throughout the domain and electrons are injected at different rates (controlled by the electron emission density n_e). A configuration including ionisation processes induced by an electron (jet extraction) flow is discussed in Sec. 6.2. Section 6.3 summarises a third configuration with a variation of the ion inflow condition while the electron inflow rate is constant.

Table 6.1: Summary of key configurations for jet extraction simulations.

#	$n_e\ [m^{-3}]$	$n_i\ [m^{-3}]$	Ionisation
1	$10^{14}...4 \cdot 10^{16}$	10^{16} uniformly distrib., no inflow	No
2	$4 \cdot 10^{16}$	10^{16} uniformly distrib., no inflow	Yes
3	$4 \cdot 10^{16}$	No ion background, two inflow BCs	No

6.1 Jet Simulation 1

The first simulations focus on the electron behavior with different electron emission densities since the effective ionisation rate inside the plasma core is unknown,. Due to the greatly different particle masses the electron velocity is typically much higher than the ion velocity. The huge amount of output data permits either electron or ion data to be saved per simulation run. Correspondingly, either electron or ion positions can be visualised although both species are simulated.
The simulations are performed with the same configuration as described in section 5.1 with the final mesh. Ions are uniformly distributed in the simulation region to define a starting condition according to the ”time averaged” oscillating motion of the ions around the center[1]. The electrons are emitted in a small box which represents an ”electron reservoir”. That means, it is assumed that electrons are mainly formed by ionisation of atoms and ions in the center of the cathode where the kinetic energy

[1] Means, velocity is zero.

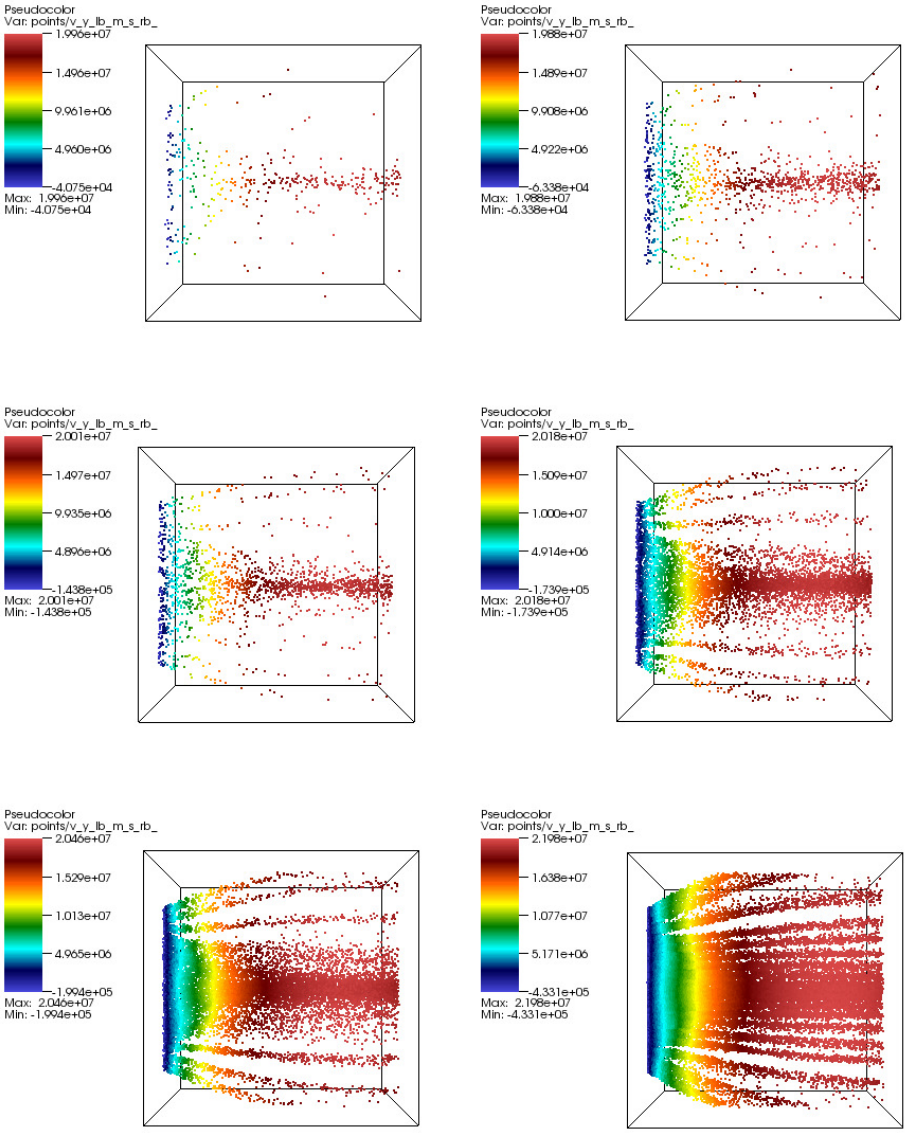

Figure 6.1: Electron motion at different electron emission densities n_e at $t_{end} = 8ns$. The colors represent the particle's velocities in y direction. TL: $n_e = 10^{14}m^{-3}$, TR: $n_e = 5 \cdot 10^{14}m^{-3}$, CL: $n_e = 10^{15}m^{-3}$, CR: $n_e = 5 \cdot 10^{15}m^{-3}$, BL: $n_e = 10^{16}m^{-3}$, BR: $n_e = 4 \cdot 10^{16}m^{-3}$.

of the incoming ions should be maximal [4].
A detailed overview of the variational studies is given in Fig. 6.1 which shows the electron particle distributions and corresponding velocities at $t_{end} = 8ns$.

Analysis of the simulations indicates that the non-symmetric field leads initially to a creation of an electron jet. For small electron emission densities, the particles move even exactly on the electric field lines that start in the inner sphere. Self-fields of

the particles increase within the particle inflow region when the non-neutral density becomes higher. Consequently, the force of the self-fields exceeds the force of the external field and the electrons move also on other lines. The reason for electrons moving on straight lines as observable in Fig. 6.1 shows is that the preparatory simulations for the identification of a proper spatial resolution (see Sec. 5) do not match the simulation conditions. The conclusion is that either the preparatory mesh resolution simulation needs additional adaptation to final simulation conditions, or this type of preparatory work needs to be considered as part of an iterative procedure. Due to the down-sizing of the simulation domain this appears to be indeed a highly iterative process simply because it is not known where the secondary plasma core electrons are produced exactly and at which rate. Hence, the spatial resolution identified is a function of the defined plasma core conditions wich are, however, unknown. In fact, a mesh refinement in the inner region would lead to a better resolution of the electric

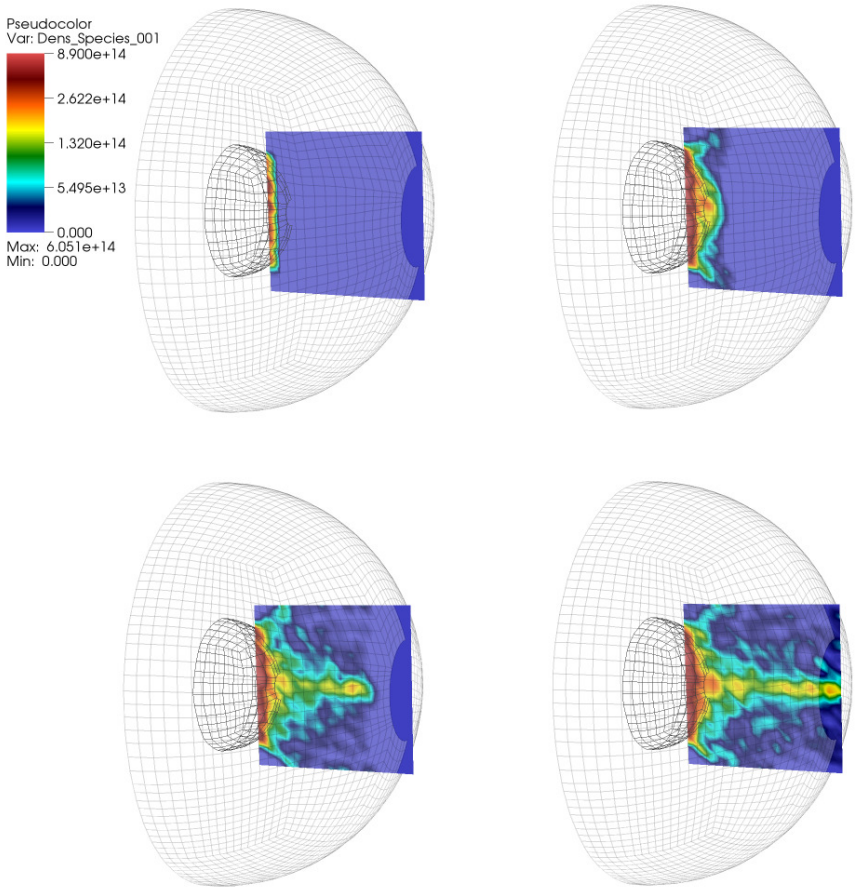

Figure 6.2: Temporal evolution of the electron density in the simulation region for $n_e = 4 \cdot 10^{16} m^{-3}$. TL: $0.43ns$, TR: $1.5ns$, BL: $2.6ns$, BR: $5.2ns$.

field in the region which dominates the electron movement. Consequently, the electron streamlines would not be determined by the first cell the electrons reach when leaving the inner sphere. Therefore, the straight trajectories would not be formed.
The temporal evolution of the electron density is exemplarily shown in Fig. 6.2. An electron jet is clearly visibly. However, according to experimental results also an ion jet extraction is expected. To study the ion movement it is necessary to increase the overall simulation time due to their significantly lower mobility. The results of the elongated simulation time (24h with 32 processes) are shown in Fig. 6.3. A region next to the outer sphere is visible in which the external electric fields and the space charge of the ions cancel out each other. Uniformly distributed ions on the left hand side of this region are all accelerated towards the IEC center. Consequently, an ion jet is not formed. More interesting is the ion behavior on the right hand side of this region. The ions do not form a jet but they are moving against the external electric field. This is clear evidence that the potential distribution inside the plasma core is necessary for a physically correct simulation in which the ions should get accelerated against the external electric field. However and as mentioned already, the simulation of the whole IEC is not feasible during the project time with the given code although highly accurate. Therefore, other inflow and boundary conditions shall be identified, certainly the uniform ion distribution is considered oversimplified.

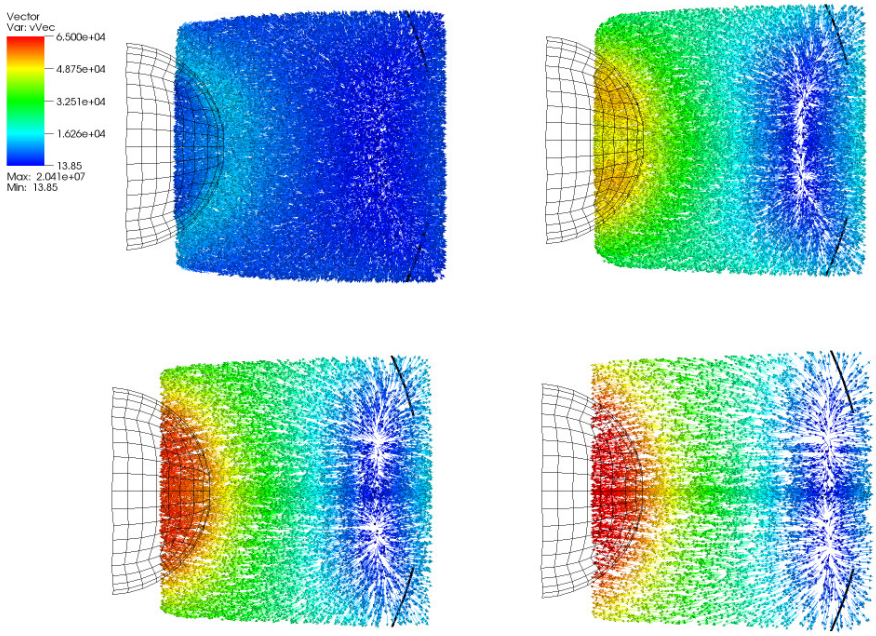

Figure 6.3: Temporal evolution of the ion velocity vectors for uniformly distributed ions $n_i = 8 \cdot 10^{16}\,\mathrm{m}^{-3}$. TL: $70\,\mathrm{ns}$, TR: $400\,\mathrm{ns}$, BL: $600\,\mathrm{ns}$, TR: $850\,\mathrm{ns}$

6.2 Jet Simulation 2

Simulations with the CMC method considering electron impact ionisation according to $e + Ar \rightarrow 2e + Ar^+$ are performed on basis of the previously mentioned particle density distributions. Neutral background density is $1.93 \cdot 10^{20} m^{-3}$. The results are depicted in Fig. 6.4. Evidently, under the given set of parameters a huge number of ionisation processes take place which slow down the simulation and extremely increase memory consumption due to newly created particles. Also, the electron jet disappears after a while presumably due to the increasing electrostatic forces generated by the newly born ions. Significantly more electrons than ions leave the system, leaving the heavy ions behind which tear apart the upcoming jet electrons. In total, the resulting plasma state does not match the expectations. An unlucky combination of simulation parameters leads to this result: Particle densities, spatial distribution, as well as energy distribution are based on estimates and guesses and not on measurements or somehow verified numbers. Also, the simulated domain is too small to be able to let inside particles *see* the electrostatic charge of initially left electrons and the respective response of the plasma core potential distribution. Additionally, chemical reactions (apart from ionisation) are neglected for the sake of simplicity. This has unfavorable side effects:

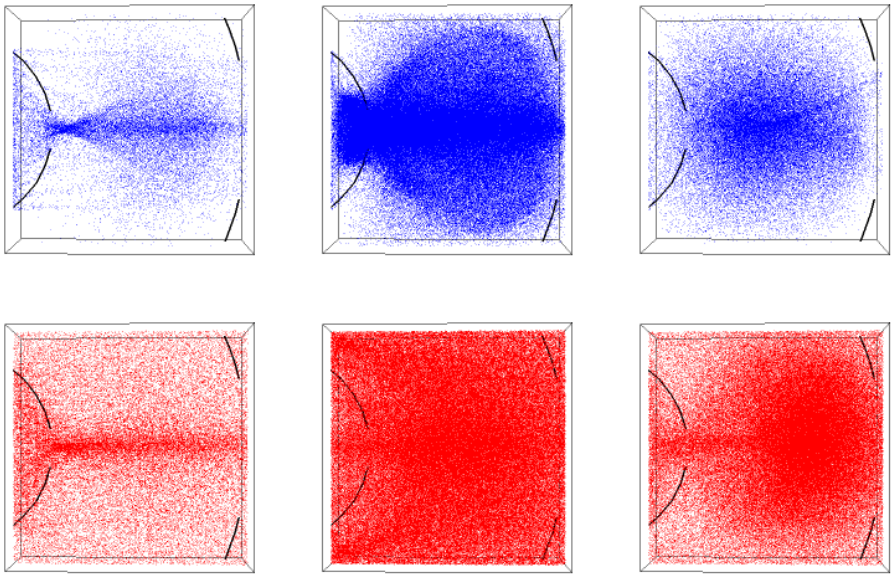

Figure 6.4: Electron and ion motion with enabled Argon ionisation. Blue points are electrons, red points are ions. The figure bottom left shows the huge number of ionisations on the trajectory of the electron jet. TL: $108ns$, TM: $288ns$, TR: $414ns$, BL: $126ns$, BM: $423ns$, BR: $684ns$

- Ignoring excitation means that the electron energy is too high and by Coulomb coupling also the ion energy.
- Ignoring charge exchange means that the ion energy is too high and by Coulomb coupling also the electron energy.

Both side effects are in favor of electron impact induced ionisation processes, increasing the system particle number even more. However, the explosion of charged particle number is considered mainly driven by the non-extraction of ions (see explanations above). Although an electron jet has been formed, the ions do not find their way out of the system fast enough which couples back to the electron jet, leading to these results. Due to the presumably dominant importance of inflow and boundary conditions compared to the consideration of complex chemistry models, all subsequently presented simulation results including the variation of boundary conditions are without chemistry at all.

6.3 Jet Simulation 3

Considering the results in chapter 6.1, the starting conditions of the ions are changed. Geometry and external electric field remain unchanged. The electrons are still emitted through the "electron reservoir" 6.1 with a density of $n_e = 4 \cdot 10^{16}\,\mathrm{m}^{-3}$. Ions are now emitted in two modes and are not further uniformly distributed in the simulation region. The first mode is the quasi neutral mode. In every time step, the same number of electrons and Argon ions is emitted within the "electron reservoir" region. This leads on one hand to an electrically neutral plasma that is emitted but also to a temporarily monotone increasing ion density in the inflow region which is a consequence of the low ion mobility.
The second mode is the mode of constant ion density in the inflow region. Here, the number of inserted ions is smaller than the number of inserted electrons. This results in a constant ion density in the inserting region, but also to a strong violation of quasi-neutrality, yielding a non-neutral plasma.

6.3.1 Quasi-neutral inflow condition

The simulation's outcome with respect to the applied quasi-neutral inflow condition is not satisfactory. The electric field is extremely small in the inner sphere. Hence, the quasi neutral plasma leads to almost no acceleration of the particles leading to a lack in visible particle movement even after a run time of 24h on 64 processes (simulated time $\approx 3\,\mu\mathrm{s}$). These simulations are not followed further.

6.3.2 Constant ion density inflow condition

With this inflow condition less ions than electrons are injected. The ion density in the inflow region is constant ($n_i = 4 \cdot 10^{16} m^{-3}$). Figure 6.5 shows how the electron jet is formed.

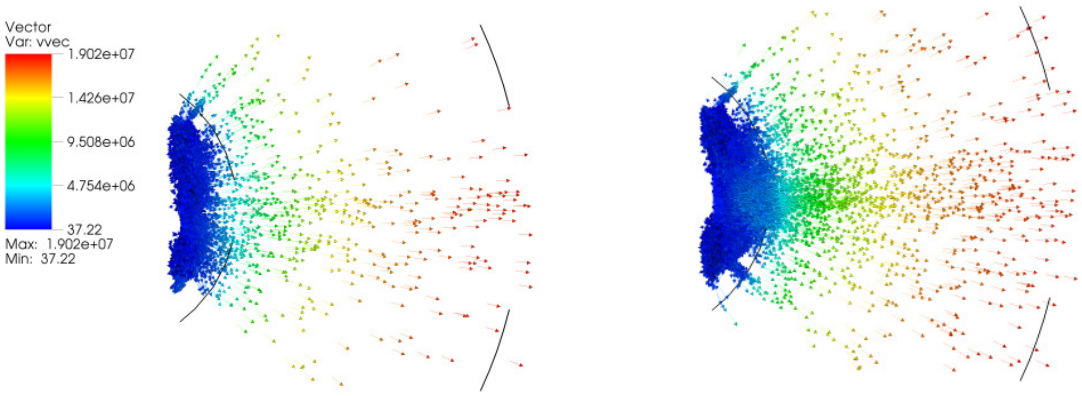

Figure 6.5: Electron motion in constant density inflow mode. Left: $930\,\mathrm{ns}$, Right: $5.3\,\mu\mathrm{s}$

Figure 6.6 displays the temporal evolution of ions in the inner sphere (inflow region) after a run time of 120h with 32 processes. Due to the non-neutrality of the plasma, a strong force acts on the ions. This evokes an ion movement which looks like the expected behavior. The ions move to the hole of the inner sphere (cathode) and also a focusing effect of the ions can be observed. However, at some moment in time (see Fig. 6.6), more and more ions start to get accelerated towards the cathode's center. In fact, the ion expansion stagnates. The dynamics of this asymptotic slowing-down makes it questionable whether further simulation time would lead to the envisaged observation. Given that and in combination with reaching budget limits the simulations under the given parameter settings (including the inflow boundary conditions) are not further continued.
The equilibrium-like stagnation is caused by the number of ions that is inserted and the number of ions that leave the region towards the middle point. At this point, the ion density does not increase anymore. This means, the space charge in the inflow region also stagnates and the electric field caused by the space charge is not high enough to overcompensate the external field. The field overcompensation would lead to a jet extraction of the ions because the external electric field is minimal close to the holes. Thus, the field lines (as shown in Fig. 4.4) would be the ion trajectories of minimal expenditure of energy.
It is expected that the symmetric space charges of the regions that are not simulated should increase the described effect and contribute to the formation of an ion jet.

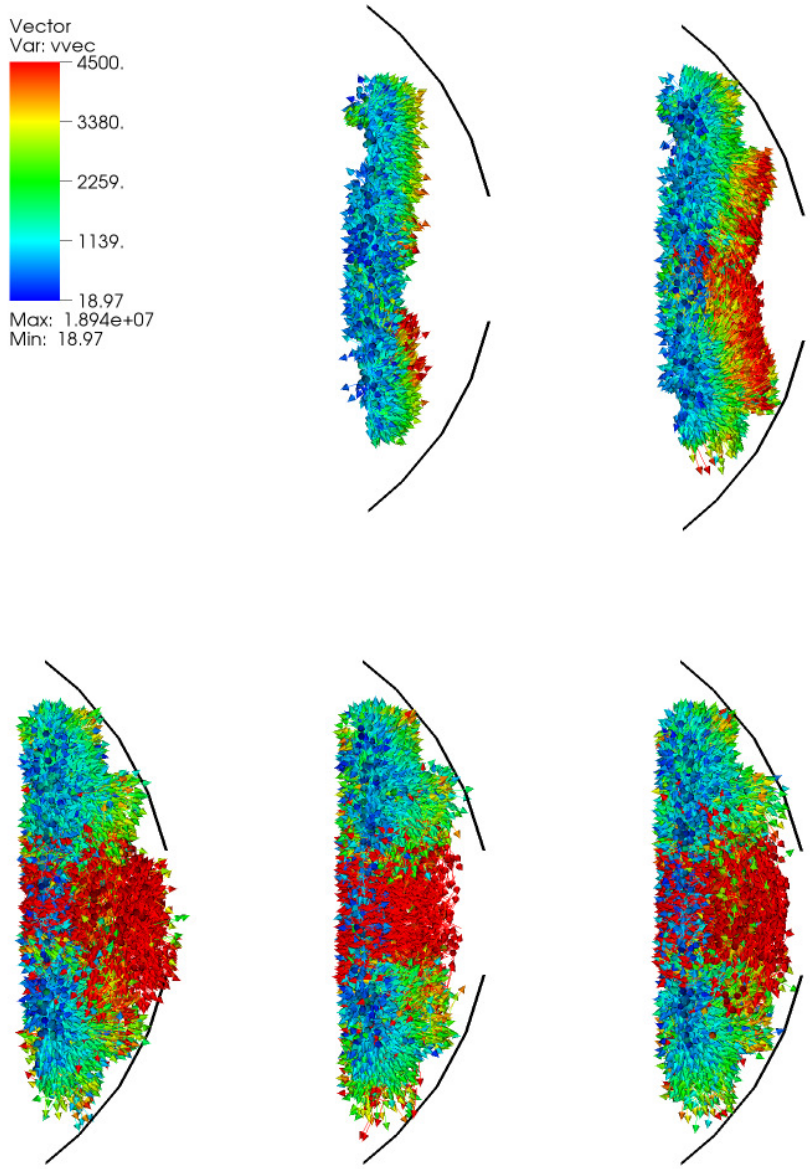

Figure 6.6: Temporal evolution of the ion movement of the constant ion density mode in the inner sphere. TL: $0.69\,\mu$s, TR: $1.35\,\mu$s, BL: $2.74\,\mu$s, BM: $3.34\,\mu$s, BR: $5.48\,\mu$s

7 Summary and Conclusions

A sub-domain of a spherical Inertial Electrostatic Confinement thruster was modeled and simulated with a fully kinetic particle based software framework. Externally applied electric fields resulting from electrode geometries and voltages were modeled via OpenFoam, imported into the kinetic code, and treated as local background fields. Additional electric field information is provided due to the non-collisional interaction between charged plasma particles. The full set of Maxwell's equations was solved to derive resulting forces acting on the particles, thereby enabling a self-consistent treatment.
The electron acceleration as the presumably initialising element of the overall jet extraction was recovered by the kinetic simulations. However, due to issues related to some code modeling elements, the complete jet extraction including ions (which provide the main thrust) was not observed. Hence, we conclude that our simulations provide additional evidence which supports the common theory - that electrons are overcoming the potential barrier. Further elements of the beam extraction hypothesis cannot be confirmed, but also not refuted. Consequently, the main objective of this study - the kinetic simulation of an IEC jet extraction, was achieved only partially.
Limiting factors in the modeling are mainly related to the accuracy of the PIC solver which, in its current state, solves the full set of Maxwell equations and, therefore, demands temporal resolution of the vacuum speed of light in the smallest cell in the whole simulation domain. This leads to extremely small time step sizes and, correspondingly, to high computational needs. Although it was possible to further reduce those during the Ariadna project (e.g. no Coulomb collisions, reduction of computational domain) only a limited amount of physical time could be reproduced despite the use of a multi-processor computer architecture.
The reduction of the computational domain reduced the computational needs significantly but this approach imposed the definition of an inflow boundary condition which has a severe impact on the simulation result. As suggested by literature, the behavior of the electrons close to the inner grid opening is driven by the local electrostatic potential which is generally unknown and key outcome of a full domain simulation. By defining two inflow boundary conditions (representing limiting cases), the potential field's shape and its impact on the electrons was defined artificially. Although the choice of the non-neutral inflow boundary condition over the neutral one based on physical considerations, this limiting case does not reproduce the jet extraction in the applied number of iterations. Note, however, this does not automatically imply that this boundary condition fails in general. A significantly longer simulation time might have led to the desired observations. However, a simulation of a larger (or even the full) physical domain with even less time steps might have lead to the desired obser-

vation as well. Both scenarios were in conflict with the available simulation budget which had to be spend mainly for the preparatory simulations for adjusting numerical parameters according to the stated problem. The following table provides an overview of the goals of this study.

Goal	**Achieved**
Defining a simulation region/ IEC test case	Done, detailed literature research
Defining particle boundary/starting conditions	Done, detailed literature research
Defining field boundary conditions	Done, using OpenFOAM solution
FP simulations - Proof of necessity	FP not considered for performance reasons, shape functions not needed under the given conditions
Mesh study	Done
Particle weighting study	Done
Decision: DSMC or CMC	Done, DSMC not feasible due to large neutral particle number
PIC + CMC simulations	Done, Results not useful due to missing recombination routine and uncertain starting conditions
PIC simulations: electron motion	**Done, jet extraction visible**
PIC simulations: ion motion	**Done, jet extraction not visible after run time of 120h with 32 processes, Longer run time and simulation of whole IEC necessary**

Figure 7.1: Overview of goal achievements.

8 Outlook

Future research activities should focus on improving computational efficiency of the PIC solver. To be precise, a pure PIC solver solving the electrostatic Poisson equation would allow to increase the global time step size by probably 2-3 orders of magnitude with respect to the herein applied PIC solver which resolves the electromagnetic wave propagation. An electrostatic PIC solver would resolve enough physical phenomena relevant to the beam extraction. In fact, this would not only allow to obtain simulation results based on significantly longer physical times but to simulate the whole domain (maybe even non-downsized) in order to provide the natural electrostatic potential distribution close to the inner grid opening. This would also relax the need for significantly more accurate particle data which needs to be provided as initial and boundary condition in the current numerical setup. However, smaller speed-up values are expected making use of the newly developed and implemented but not yet verified pseudo-electrostatic Poisson solver.
The plane which represents the exit face of the jet particles should contain some clever algorithm which is able to cope with the charges already left the domain (at least to some degree of accuracy) but still having electrostatic impact on the charges inside the domain. Currently, a charge leaving the system does not have an impact on any charge inside the domain despite the long range Coulomb potential.
Also, the role of Coulomb collisions near the inner grid opening should be studied more in detail as well as chemical reactions which affect the composition of the jet. In fact, the electron distribution function' relaxation is coupled to the chemistry due to the fact that electron induced processes are much more efficient than ion induced reactions. The inclusion of nuclear fusion reactions would allow to answer whether a mode of operation exists which justifies to operate an IEC thruster in a hybrid jet and fusion mode. Given that, a Fokker Planck solver would presumably impact on the resolution of space charge induced jet extraction processes (to get a full picture of the acceleration process), on the chemical processes along the jet stream (to assess beam properties and thrust characteristics), and on the thermalisation of highly energetic charged nuclear fusion products (to assess high order loss mechanisms and potential thermal thrust components).
Of course, a validation of a full plasma jet extraction's simulation can be realised only on basis of reliable experimental measurements of relevant quantities.

Bibliography

[1] P.T. Farnsworth. Electric discharge device for producing interactions between nuclei. US Patent 3,258,402, 1966.

[2] R. L. Hirsch. Inertial-electrostatic confinement of ionized fusion gases. *Journal of Applied Physics*, 38(11):4522–4534, 1967.

[3] R.W. Bussard and N.A. Krall. Inherent characteristics of fusion power systems: Physics, engineering and economics. *Journal Fusion Technology*, 26:1326–1336, 1994.

[4] G.H. Miley, Y. Gu, J.M DeMora, R.A Stubbers, T.A. Hochberg, J.H. Nadler, and R.A Anderl. Discharge characteristics of the spherical inertialconfinement (iec) device. *IEEE Transactions on Plasma Science*, 25(4):733–739, 1997.

[5] G.H. Miley. Plasma jet source using an inertial electrostatic confinement dischrage plasma, 2000.

[6] C.C. Dietrich. *Improving Particle Confinement in Inertial Electrostatic Fusion for Spacecraft Power and Propulsion*. PhD thesis, MIT, 2007.

[7] G.H. Miley and J. Sved. The iec star-mode fusion neutron source for naa-status and next-step designs. *Journal Applied Radiation and Isotopes*, 53:779–783, 2000.

[8] C. Syring and G. Herdrich. Development activities of an inertial electrostatic confinement device for space applications. *63rd IAC conference proceedings*, IAC-12-C4.7-C3.5.8, 2012.

[9] P.T. Farnsworth. Method and apparatus for producing nuclear-fusion reactions, 1968.

[10] Y. Gu and G.H. Miley. Experimental study of potential structure in a spherical iec fusion device. *IEEE Transactions on Plasma Science*, 28(1):331–346, 2000.

[11] J.H. Nadler, E.D Yoder, C. Hunsicker, and G.H. Miley. Experimental investigation of unique plasma jets for use as ion thrusters. *29th AIAA Plasmadynamics and Lasers Conference*, AIAA-98-2570, 1998.

[12] G.H. Miley, B.P Bromley, and Y. Gu. A novel iec propulsion unit for satellite applications. *AIP Conference Proceedings*, 361:1435–1439, 1996.

[13] C. Syring and G. Herdrich. Discharge and operational conditions of an inertial electrostatic confinement device. *Proceedings Joint Propulsion Conference*, AIAA-2013-4025, 2013.

[14] D. Petkow, G. Herdrich, S. Fasoulas, and M. Auweter-Kurtz. On the kinetic modeling of collisional effects relevant for non-stationary magnetoplasmadynamic thrusters. IEPC-2011-311, The 32nd International Electric Propulsion Conference, Wiesbaden, Germany, 2011.

[15] C. Cercignani. *Mathematical Methods in Kinetic Theory, Sec. Ed.* Plenum Press, New York and London, 1990.

[16] C. Cercignani, R. Illner, and M. Pulvirenti. *The Mathematical Theory of Dilute Gases*. Applied Mathematical Sciences 106. Springer Verlag, 1994.

[17] S. Rjasanow and W. Wagner. *Stochastic Numerics for the Boltzmann Equation*. Springer-Verlag Berlin Heidelberg, 2005.

[18] C.K. Birdsall and A.B. Langdon. *Plasma Physics via Computer Simulation*. Adam Hilger, Bristol, Philadelphia, New York, 1991.

[19] C.-D. Munz, P. Omnes, R. Schneider, E. Sonnendrcker, and U. Vo. Divergence correction techniques for maxwell solvers based on a hyperbolic model. *Journal of Computational Physics*, 161(2):484–511, July 2000.

[20] C.-D. Munz, P. Ommes, and R. Schneider. A three-dimensional finite-volume solver for the maxwell equations with divergence cleaning on unstructured meshes. *Computer Physics Communications*, 130(12):83–117, July 2000.

[21] J. Neudorfer, A. Stock, J. Flamm, F. Hindenlang, G. Gassner, C.-D. Munz, R. Schneider, and S. Roller. Numerical investigation of high-order gyrotron mode propagation in launchers at 170 ghz. *IEEE Transactions on Plasma Science*, 40(6):1512–1521, 2012.

[22] A. Stock. *A High-Order Particle-in-Cell Method for Low Density Plasma Flow and the Simulation of Gyrotron Resonator Devices*. PhD thesis, Institute of Aerodynamics and Gas Dynamics, Universität Stuttgart, 2013.

[23] F. Hindenlang, G. J. Gassner, C. Altmann, A. Beck, and M. Staudenmaier. Explicit discontinuous galerkin methods for unsteady problems. *Computers & Fluids*, 61:86–93, 2012.

[24] G.A. Bird. Approach to translational equilibrium in a rigid sphere gas. *Physics of Fluids*, 6:1518–1519, 1963.

[25] G.A. Bird. *Molecular Gas Dynamics and the Direct Simulation of Gas Flows*. Clarendon Press, Oxford, 1994.

[26] D. Petkow. *Partikelbasierte Modellierung und Simulation von hochverdünnten Plasmaströmungen*. PhD thesis, Institute of Space Sytems, Universität Stuttgart, 2011.

[27] F. Bozsak. Erweiterung des partikelverfahrens piclas hinsichtlich c-f-basierter atomarer an- und abregungsprozesse. Study thesis irs 08-s-28, Institute of Space Systems, Universität Stuttgart, 2008.

[28] C. Syring. Beitrag zur vollkinetischen simulation der entladung des gepulsten plasmatriebwerkes add simplex. Diploma thesis, Institute of Aerospace Thermodynamics, Universität Stuttgart, July 2009.

[29] K. Nanbu. Theory of cumulative small-angle collisions in plasmas. *Phys. Rev. E*, 55:4642–4652, Apr 1997.

[30] A. V. Bobylev and K. Nanbu. Theory of collision algorithms for gases and plasmas based on the boltzmann equation and landau-fokker-planck equation. *Phys. Rev. E*, 61:4576–4586, 2000.

[31] D.J. Meeker, J.T. Verdeyen, and B.E. Cherrington. Measurement of electron density in a cylindrical inertial electrostatic plasma confinement device. *Journal of Applied Physics*, 44:5347–5355, 1973.

[32] T.J. Dolan. Electrostatic inertial plasma confinement. *Journal of Applied Physics*, 43:1590–1600, 1972.

[33] C. C. Dobson and I. Hrbud. Electron density and two-channel neutron emission measurements in steady-state spherical inertial-electrostatically confined plasmas, with reviwe of the one-dimensional kinetic model. *Journal of Applied Physics*, 96(1):94–108, 2004.

[34] T.A. Thorson. Convergence, electrostatic potential, and density measurements in a spherically convergent ion focus. *Physical Plasmas*, 4(1):4–15, 1997.

[35] M.A. Lieberman and A.J. Lichtenberg. *Principles of Plasma Discharges and Materials Processing*. Wiley,J., 2 edition, 2005.

[36] M. A. Grado-Caffaro and M. Grado-Caffaro. Fowler-nordheim electron tunneling under very intense electric field. *Optik*, 121:2001–2002, 2010.

[37] N.W. Ashcroft and D. Mermin. *Solid-State Physics*. Cengage Learning Emea, 1976.

[38] H. Ibach and H. Lüth. *Solid-State Physics - An introduction to principles of materials science*. Springer-Verlag, 7 edition, 2009.

[39] J. Orloff. *Handbook of charged particle optics*. CRC Press, Taylor & Francis Group, 2 edition, 2009.

[40] A. Bogaerts, E. Neyts, R. Gijbels, and J. v.d.Mullen. Gas discharge plasmas and their applications. *Spectrochimica Acta Part B*, 57:609–658, 2002.

[41] M. H. Mittleman and L. Wilets. Statistical treatment of ionization in atomic collisions. *Physical Review*, 154(1):12–16, 1967.

[42] R.M. Meyer. *Inertial electrostatic confinement theoretical and experimental studies of spherical devices*. PhD thesis, Faculty of nuclear engineering,University of Missouri-Columbia,USA, 2007.